This article was downloaded by:
On: *22 January 2011*
Access details: *Access Details: Free Access*
Publisher *Taylor & Francis*
Informa Ltd Registered in England and Wales Registered Number: 1072954 Registered office: Mortimer House, 37-41 Mortimer Street, London W1T 3JH, UK

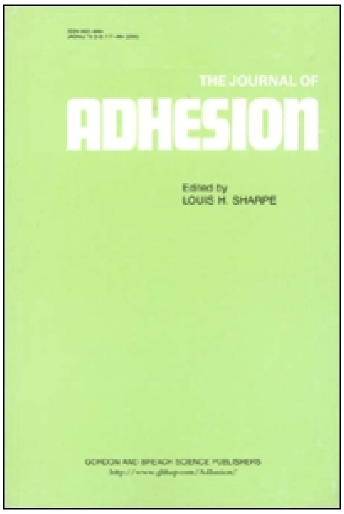

The Journal of Adhesion

Publication details, including instructions for authors and subscription information:
http://www.informaworld.com/smpp/title~content=t713453635

Aerosol Particle Removal and Re-entrainment in Turbulent Channel Flows - A Direct Numerical Simulation Approach

Haifeng Zhang[a]; Goodarz Ahmadi[a]
[a] Department of Mechanical and Aeronautical Engineering, Clarkson University, Potsdam, NY, USA

To cite this Article Zhang, Haifeng and Ahmadi, Goodarz(2000) 'Aerosol Particle Removal and Re-entrainment in Turbulent Channel Flows - A Direct Numerical Simulation Approach', The Journal of Adhesion, 74: 1, 441 — 493

To link to this Article: DOI: 10.1080/00218460008034541

URL: http://dx.doi.org/10.1080/00218460008034541

PLEASE SCROLL DOWN FOR ARTICLE

Full terms and conditions of use: http://www.informaworld.com/terms-and-conditions-of-access.pdf

This article may be used for research, teaching and private study purposes. Any substantial or systematic reproduction, re-distribution, re-selling, loan or sub-licensing, systematic supply or distribution in any form to anyone is expressly forbidden.

The publisher does not give any warranty express or implied or make any representation that the contents will be complete or accurate or up to date. The accuracy of any instructions, formulae and drug doses should be independently verified with primary sources. The publisher shall not be liable for any loss, actions, claims, proceedings, demand or costs or damages whatsoever or howsoever caused arising directly or indirectly in connection with or arising out of the use of this material.

J. Adhesion, 2000, Vol. 74, pp. 441 - 493
Reprints available directly from the publisher
Photocopying permitted by license only

Aerosol Particle Removal and Re-entrainment in Turbulent Channel Flows – A Direct Numerical Simulation Approach

HAIFENG ZHANG and GOODARZ AHMADI*

Department of Mechanical and Aeronautical Engineering,
Clarkson University, Potsdam, NY 13699-5727, USA

(Received 19 July 1999; In final form 14 February 2000)

Aerosol particle removal and re-entrainment in turbulent channel flows are studied. The instantaneous fluid velocity field is generated by the direct numerical simulation (DNS) of the Navier-Stokes equation *via* a pseudospectral method. Particle removal mechanisms in turbulent channel flows are examined and the effects of hydrodynamic forces, torques and the near-wall coherent vorticity are discussed. The particle resuspension rates are evaluated, and the results are compared with the model of Reeks. The particle equation of motion used includes the hydrodynamic, the Brownian, the shear-induced lift and the gravitational forces. An ensemble of 8192 particles is used for particle resuspension and the subsequent trajectory analyses. It is found that large-size particles move away roughly perpendicular to the wall due to the action of the lift force. Small particles, however, follow the upward flows formed by the near-wall eddies in the low-speed streak regions. Thus, turbulent near-wall vortical structures play an important role in small particle resuspension, while the lift is an important factor for re-entrainment of large particles. The simulation results suggests that small particles (with $\tau_p^+ \leq 0.023$) primarily move away from the wall in the low-speed streaks, while larger particles (with $\tau_p^+ \geq 780$) are mostly removed in the high-speed streaks.

Keywords: Particle removal; Re-entrainment; Turbulence; Direct simulation; Removal trajectories; Resuspension

---

*Corresponding author. Tel.: 315-268-2322, Fax: 315-268-6438, e-mail: ahmadi@clarkson.edu

INTRODUCTION

Particle detachment from surfaces has increasingly become the subect of considerable attraction because of its importance in the semiconductor and imaging industries. Numerous studies concerning the particle detachment mechanisms from various surfaces have been reported by Mittal [1]. Extensive reviews of the particle adhesion mechanism have been provided by Corn [2], Krupp [3], Visser [4], Tabor [5], Bowling [6], and Ranade [7]. Accordingly, the van der Waals force makes the major contribution to the particle adhesion force on a surface under dry conditions.

The effect of contact deformation on adhesion was first considered by Derjaguin [8]. More recently, Johnson *et al.* [9] used the surface energy and surface deformation effects to develop an improved contact model called the JKR theory. According to this model, at the moment of separation, the contact area does not disappear entirely; instead, a finite contact area exists.

Derjaguin *et al.* [10] developed a new theory based on the Hertzian profile assumption. In this model (the so-called DMT theory) the force required to detach the particle from the surface is 4/3 as large as in the JKR theory. Further progress was reported by Muller [11, 12]. Accordingly, for a system that has a high Young's modulus, low surface energy, and small-diameter particles, the DMT theory applies. In contrast, for a system that has a low Young's modulus, high surface energy, and large particle size, the JKR theory is more suitable. Recently, Maugis [13] analyzed the adhesion of spheres to plane surfaces based on the assumption that the adhesion force is constant in the region near the contact boundary. His analytical results clearly show the transition between the JKR and DMT theories. The JKR theory is further generalized by Maugis and Pollock [14] by allowing for plastic deformation.

Tsai *et al.* [15] studied the elastic flattening and particle adhesion and argued that the JKR theory is not correct for hard systems, and also that there is a violation of the static equilibrium in the DMT theory. They proposed a new (TPL) model which considers the effect of material properties in the deformation and adhesion force of particle-surface systems. Rimai *et al.* [16] performed a series of experimental studies and reported significant effects of the Young's modulus and material properties on the surface-force-induced contact radii of spherical particles. Soltani and Ahmadi [17, 18] studied the particle removal mechanisms from smooth and rough walls subject to substrate accelerations.

Numerous experimental and computational studies related to particle transport in turbulent flows were reported in the literature (Hinze [19], Ahmadi [20]). Extensive reviews on particle removal process from surfaces were provided by Healy [21], Sehmel [22], Nicholson [23], and Smith *et al.* [24]. Braaten *et al.* [25] performed an experimental study of particle re-entrainment in turbulent flow. They concluded that ejection-sweep events and macrosweep flow patterns near a wall strongly affect the particle resuspension process. However, based on their flow visualization experiments, Yung *et al.* [26] reported that the bursting phenomenon has a small effect on entrainment of particles within the viscous sublayer.

A sublayer model for particle resuspension and deposition in turbulent flows was proposed by Cleaver and Yates [27–29]. In particular, they suggested that the particle entrainment most likely results from the wall ejection events, while their deposition occurs by the inrush process. A dynamic model for the long-term resuspension of small particles from smooth and rough surfaces in turbulent flow was developed by Reeks *et al.* [30] and Reeks and Hall [31]. A kinetic model for particle resuspension was proposed by Wen and Kasper [32] and compared with the data from industrial high-purity gas systems and with controlled experiments using Latex particles of 0.4 – 1 μm. Wang [33] studied the effect of inceptive motion on particle detachment from surfaces and concluded that the removal of spherical particles is more easily achieved by the rolling motion, rather than sliding or lifting. This result is consistent with the experimental observation of Masironi and Fish [34]. A flow-structure-based model for turbulent resuspension was developed by Soltani and Ahmadi [35, 36].

A series of direct numerical simulations (DNS) of particle deposition in wall-bounded turbulent flows were performed by McLaughlin [37] and Ounis *et al.* [38, 39]. These studies were concerned with providing insight into the particle deposition mechanisms in turbulent flows. Brooke *et al.* [40] performed detailed DNS studies of vortical structures in the viscous sublayer. Recently, Pedinotti *et al.* [41] used the DNS to investigate the particle behavior in the wall region of turbulent flows. They reported that an initially uniform distribution of particles tends to segregate into low speed streaks and resuspension occurs by particles being ejected from the wall. The DNS simulation was used by Soltani and Ahmadi [42] to study the particle entrainment process in a turbulent channel flow. They found that the wall coherent structure plays a dominant role in the particle entrainment process.

Squires and Eaton [43] simulated a homogeneous, isotropic, non-decaying turbulent flow field by imposing an excitation at low wave numbers, and studied the effects of inertia on particle dispersion. They also used the DNS procedure to study the preferential micro-concentration structure of particles as a function of the Stokes number in turbulent, near-wall flows [44]. Rashidi *et al.* [45] performed an experiment to study the particle-turbulence interactions near a wall. They reported that the particle transport is mainly controlled by the turbulence burst phenomena.

In this work, the particle removal mechanism from the smooth surface in turbulent channel flows is studied. The theories of rolling and sliding detachments are used, and the critical removal condition is analyzed. Effects of various forces and turbulent near-wall coherent eddies on the turbulent resuspension process are studied. An ensemble of 8192 particles is used in these simulations, and it is shown that the turbulent near-wall vortical structure and the lift force, respectively, play important roles on small and large particle re-entrainment and resuspension processes.

TURBULENT FLOW FIELD VELOCITY

The instantaneous fluid velocity field in the channel is evaluated by the direct numerical simulation (DNS) of the Navier–Stokes equation. It is assumed that the fluid is incompressible, and a constant mean pressure gradient in the x-direction is imposed. The corresponding governing equations of motion are:

$$\nabla \cdot \mathbf{u} = 0 \tag{1}$$

$$\frac{\partial \mathbf{u}}{\partial t} + \mathbf{u} \cdot \nabla \mathbf{u} = \nu \nabla^2 \mathbf{u} - \frac{1}{\rho^f} \nabla P \tag{2}$$

where $\mathbf{u} = (u_x, u_y, u_z)$ is the fluid velocity vector, P is the pressure, ρ^f is the density, and ν is the kinematic viscosity. The fluid velocity is assumed to satisfy the no-slip boundary conditions at the channel walls. In the simulations, a channel that has a width of 250 wall units, and a 630 × 630 periodic segment in x- and z-directions is used. The schematics of the flow domain and the periodic cell is shown in Figure 1a. A 16 × 64 × 64 computational grid in the x-, y- and z-directions is also employed. The grid spacing in the x- and z-directions is constant, while the variation of grid points in the y-direction is represented by the Chebyshev series. The distance of the ith grid point in the y-direction from the centerline is given as

$$y_i = \frac{h}{2}\cos(\pi i/M), \quad 0 \le i \le M \tag{3}$$

Here h is the channel height, $M = 64$, and there are 65 grid points in the y-direction.

The channel flow code used in this study is the one developed by McLaughlin [37]. To solve for the velocity components by pseudospectral methods, the fluid velocity is expanded in a three-dimensional Fourier–Chebyshev series. The fluid velocity field in the x- and z-direction is expanded by Fourier series, while in the y-direction the

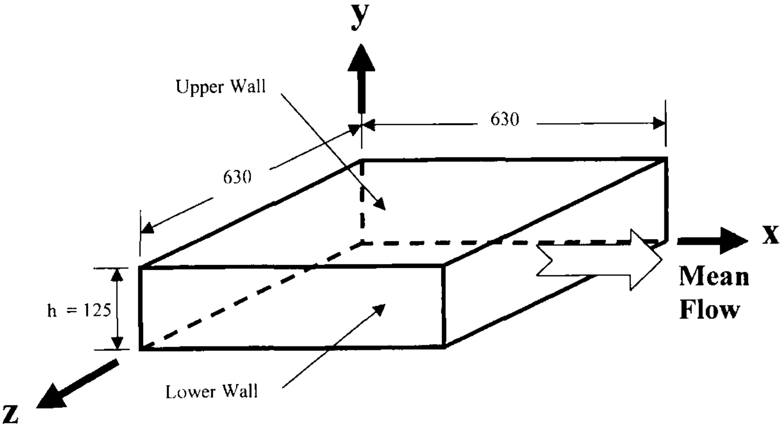

FIGURE 1a Schematics of the channel flow and the computational periodic cell used.

Chebyshev series is used. The code uses an Adams–Bashforth–Crank–Nickolson (ABCN) scheme to compute the nonlinear and viscous terms in the Navier–Stokes equation and performs three fractional time steps to forward the fluid velocity from time step (N) to time step $(N+1)$. The details of the numerical techniques were described by McLaughlin [37]. In these computer simulations, wall units are used; and all variables are nondimensionalized in terms of shear velocity, u^*, and kinematic viscosity, ν.

MacLaughlin [37] showed that the near wall root-mean-square fluctuation velocities as predicted by the present DNS code are in good agreement with the high resolution DNS code of Kim *et al.* [46]. Zhang and Ahmadi [47] showed that the present DNS with a grid size of $16 \times 64 \times 64$ can produce first-order and second-order turbulence statistics that are reasonably accurate when compared with the results of high resolution grids of $32 \times 64 \times 64$ and $32 \times 128 \times 128$. In this paper, for the sake of computational economy, the coarser grid is used.

Figure 1b shows the geometry of the flow and a sample instantaneous velocity field at $t^+ = 100$ in different planes. While the velocity field in the $y-z$ plane (at $x^+ = 157.5$) shown in Figure 1b has a random pattern, near-wall coherent eddies and flow streams towards and away from the wall can be observed from this figure. The random deviations from the expected mean velocity profile are clearly seen from Figures 1c, and d shows that the flow is predominantly in the x-direction. The near wall low- and high-speed streaks are also noticeable from this figure.

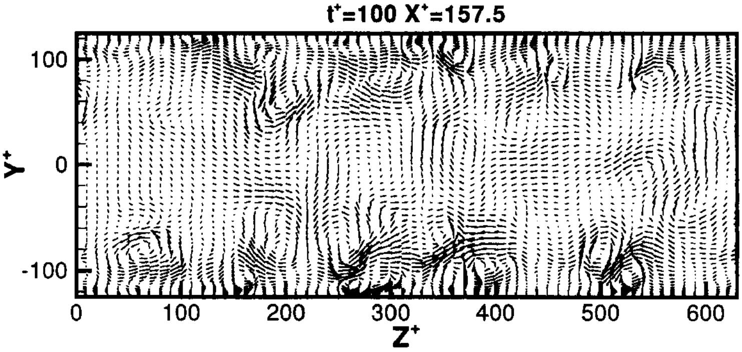

FIGURE 1b Sample velocity vector plot in the $y-z$ plane.

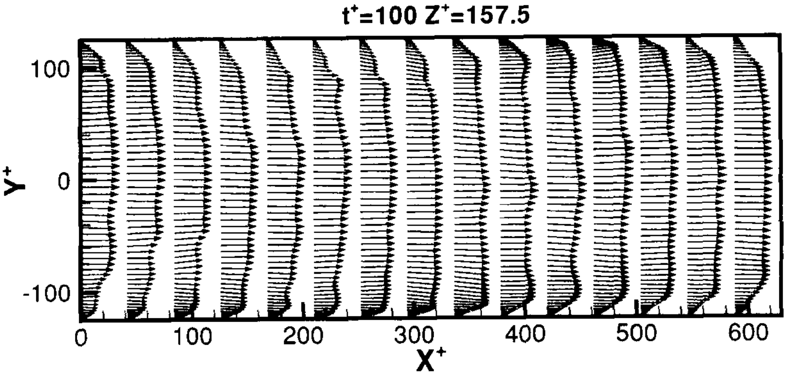

FIGURE 1c Sample velocity vector plot in the $x-y$ plane.

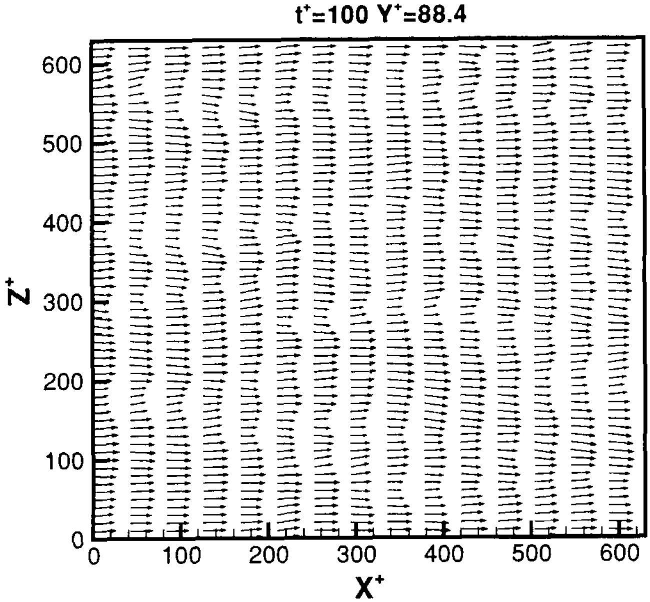

FIGURE 1d Sample velocity vector plot in the $x-z$ plane.

ADHESION MODELS

JKR Model

The Hertz contact theory is modified in this model by taking into account the surface energy effects and by allowing for the deformation of the particle and substrate surfaces. Accordingly, a finite contact area forms and the radius of the contact circle, a, is given as

$$a^3 = \frac{d}{2K}\left[P + \frac{3W_A\pi d}{2} + \sqrt{3\pi W_A dP + \left(\frac{3\pi W_A d}{2}\right)^2}\,\right] \tag{4}$$

where

$$K = \frac{4}{3}\left[\frac{(1-\nu_1^2)}{E_1} + \frac{(1-\nu_2^2)}{E_2}\right]^{-1} \tag{5}$$

is the composite Young's modulus. Here, d is the diameter of the spherical particle, W_A is the thermodynamic work of adhesion, P is the applied normal load, and ν_i and E_i are, respectively, the Poisson's ratio and the Young's modulus of material i ($i = 1$, or 2).

According to the JKR model, to detach a sphere from a plane surface, the required pull-off force, F_{P_o}, is given by

$$F_{P_o}^{\mathrm{JKR}} = \frac{3}{4}\pi W_A d \tag{6}$$

At the moment of separation, the contact radius is finite and is given by

$$a = \frac{a_0}{4^{1/3}} \tag{7}$$

where a_0 is the contact radius at zero applied load given as

$$a_0 = \left(3\pi W_A d^2/2K\right)^{1/3} \tag{8}$$

For a number of common interfaces, the corresponding material properties are listed in Table I. In this table, A is the Hamaker constant, and k is the friction coefficient.

TPL Model

Based on a detailed molecular interaction analysis, Tsai *et al.* [15] found the following equation for the force required to detach a particle

TABLE I Material properties

Material	E $(10^{10}\,N/m^2)$	A $(10^{-20}\,J)$	W_A $(10^{-3}\,J/m^2)$	ρ $(10^3\,kg/m^3)$	ν_i	k
Silicon - Silicon	17.90	23.50	38.9	2.3	0.27	0.9
Graphite - Graphite	67.50	46.90	77.75	2.2	0.16	0.1
Copper - Copper	13.00	28.30	46.91	8.89	0.34	1.6
Glass - Glass (dry air)	6.9	8.5	14.1	2.18	0.2	0.9
Glass - Glass (moist air)	6.9	320	530	2.18	0.2	0.9
Steel - Steel	21.5	21.2	35	7.84	0.28	0.58
Glass - Steel	–	–	150	–	–	0.6
Polyst - Polyst	0.28	6.37	10.56	1.05	0.33	0.5
Polyst - Nickel	–	14.27	23.65	–	–	–
Rubber - Rubber	2.4e-4	20.5	34	1.13	0.5	0.8

from a plane surface:

$$F^{\mathrm{TPL}}_{P_o} = F_0\{0.5\exp[0.124(\coprod - 0.01)^{0.439}] + 0.2\coprod\} \tag{9}$$

where the adhesion parameter, $\coprod$, is defined as

$$\coprod = \left[\frac{25A^2 d}{288 z_0^7 K^2}\right]^{1/3} \tag{10}$$

and

$$F_0 = \pi W_A d \tag{11}$$

Here, z_0 is the minimum separation distance and A is the Hamaker constant. The corresponding contact radius at the moment of separation is given as

$$\frac{a}{d} = \sqrt{\frac{K_{20} z_0}{2d}} \tag{12}$$

where K_{20} is the deformation parameter at the equilibrium condition and, according to Tsai *et al.* [15], is given by

$$K_{20} = 0.885[\exp(0.8\coprod^{0.5}) - 1.0], \quad \coprod \leq 1.6 \tag{13}$$

$$K_{20} = 0.735\coprod^{0.178} + 0.52\coprod, \quad \coprod > 1.6 \tag{14}$$

The adhesion parameter, $\coprod$, for particle diameters between 0.01 and 100 μm varies from 0.01 to 5 for metals and oxides, and from 5 to 200 for polymers.

DETACHMENT MODEL

A particle may be detached from a surface when the applied forces overcome the adhesion forces. A particle may lift-off from the surface, slide over it, or roll on the surface. These detachment mechanisms have been discussed by Wang [33]. The moment and sliding detachment mechanisms which are important for particle removal by fluid flows are briefly described here.

Moment Detachment

The critical moment model for the detachment of particles from a surface was studied by Tsai *et al.* [15] and Soltani and Ahmadi [35, 36]. Figure 2 shows the geometric features of a spherical particle attached to a plane surface. A particle will be detached when the external force moment about point "*o*", which is located at the rear perimeter of the contact circle, overcomes the resisting moment due to the adhesion force. That is

$$M_t + F_t\left(\frac{d}{2} - \alpha_0\right) + F_L a \geq F_{P_0} a \qquad (15)$$

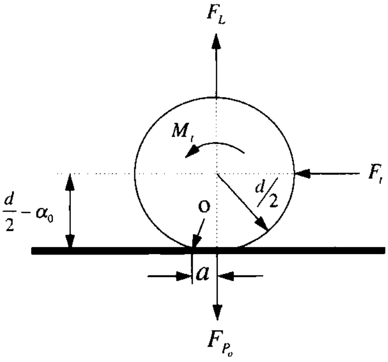

FIGURE 2 Geometric features of a spherical particle attached to a smooth surface.

where F_t is the tangential external force acting on the particle (*e.g.*, the fluid drag force), α_0 is the relative approach between the particle and surface (at equilibrium conditions), M_t is the external moment of the surface stresses about the center of the particle, F_L is the lift force, and F_{P_o} is the particle adhesion force.

Sliding Detachment

Wang [33] studied the effect of inceptive motion on particle detachment. Accordingly, the particle will be removed by sliding if

$$F_t \geq kF_{P_o} \tag{16}$$

Here F_t is external force (*i.e.*, the fluid drag force) acting on the particle parallel to the surface, and k is the coefficient of static friction.

PARTICLE EQUATIONS OF MOTION

The equations of motion for a spherical particle moving in a channel flow are given as:

$$\frac{d\mathbf{v}^+}{dt^+} = \mathbf{g}^+ + \mathbf{F}_d^+ + \mathbf{F}_L^+ + \mathbf{n}^+(t^+) \tag{17}$$

and

$$\frac{d\mathbf{x}^+}{dt} = \mathbf{v}^+ \tag{18}$$

where $\mathbf{g}^+$ is the gravity, $\mathbf{F}_d^+$ is the drag force, $\mathbf{F}_L^+$ is the lift force, and $\mathbf{n}^+(t^+)$ is the Brownian random force. (Note that only the y-component of the lift force is considered in this study.) All variables are nondimensionlized by the fluid viscosity, ν, and shear velocity, u^*. That is

$$\mathbf{x}^+ = \frac{\mathbf{x}u^*}{\nu}, \quad \mathbf{v}^+ = \frac{\mathbf{v}}{u^*}, \quad t^+ = \frac{tu^{*2}}{\nu}, \quad \mathbf{g}^+ = \frac{\nu}{u^{*3}}\mathbf{g},$$
$$\mathbf{F}_d^+ = \frac{\nu}{u^{*3}}\mathbf{F}_d, \quad \mathbf{F}_L^+ = \frac{\nu}{u^{*3}}\mathbf{F}_L \tag{19}$$

Drag Force

The combined effect of the translational motion, rotational motion and fluid shear due to the presence of the wall was studied by Goldman *et al.* [48]. For a sphere with no externally-applied torque moving in a wall-bounded channel flow, the drag force can be expressed as

$$\mathbf{F}_d = \frac{6\pi\mu a C_N}{C_c}\begin{pmatrix} C_x^w(u_x - v_x) \\ C_y^w(u_y - v_y) \\ C_z^w(u_z - v_z) \end{pmatrix} \tag{20}$$

where $\mathbf{u} = (u_x, u_y, u_z)$ is the fluid velocity, $\mathbf{v} = (v_x, v_y, v_z)$ is the particle velocity, $a = d/2$ is the particle radius, μ is the coefficient of viscosity, C_i^w is the wall correction factor, and C_c is the Cunningham correction factor given by

$$C_c = 1 + \frac{2\lambda}{d}[1.257 + 0.4\exp(-1.1d/2\lambda)] \tag{21}$$

Here, λ is the mean free path of the gas.

When the Reynolds number of the particle based on particle-fluid slip velocity is not small, the drag force deviates from the Stokes expression. The nonlinear correction coefficient to the Stokes drag is given as (Hinds [49])

$$C_N = 1 + 0.15\,\mathrm{Re}_p^{0.687} \tag{22}$$

Equation (22) agrees with experiments in the range of $1 < \mathrm{Re}_p < 200$, where Re_p is the Reynolds number of the particle defined as

$$\mathrm{Re}_p = \frac{|\mathbf{v} - \mathbf{u}|d}{\nu} \tag{23}$$

Based on a synthesis of available experimental results, Clift *et al.* [50] recommended the following nonlinear drag correction factors:

$$C_N = 1 + 0.1875\mathrm{Re}_p \quad \text{for } \mathrm{Re}_p \le 0.01 \tag{24}$$

and

$$C_N = 1 + 0.1315\mathrm{Re}_p^{0.82-0.0217\ln(\mathrm{Re}_p)} \quad \text{for } 0.01 < \mathrm{Re}_p < 20 \tag{25}$$

Combining the results of Goldman *et al.* [48, 51] and Brenner [52], Li [53] suggested for the following wall correction factors:

$$C_x^w = \frac{v_x f_x^{t*} - (f_x^{r*}/t_z^{r*})\left(v_x t_z^{t*} + (aG_x/2)t_z^{s*}\right) + yG_x f_x^{s*}}{u_x - v_x} \tag{26}$$

$$C_y^w = f_y^{t*} \tag{27}$$

$$C_z^w = \frac{v_z f_z^{t*} - (f_z^{r*}/t_x^{r*})\left(v_z t_x^{t*} + (aG_z/2)t_x^{s*}\right) + yG_z f_z^{s*}}{u_x - v_x} \tag{28}$$

where y is the distance from the particle center to the wall, G_x, G_z, are the shear rates in the streamwise and spanwise directions, $f_i^{t*}, f_i^{r*}, f_i^{s*}$, t_i^{t*}, t_i^{r*} and t_i^{s*} are the nondimensional coefficients that depend only on a/y (or δ/a) where $\delta = y - a$.

In the lubrication limit ($\delta/a \leq 0.01$) according to the asymptotic solutions of Goldman *et al.* [48], the nondimensional coefficients are given as

$$f_x^{t*} = f_z^{t*} = 0.5333 \ln(\delta/a) - 0.9588 \tag{29}$$

$$f_x^{r*} = f_z^{r*} = -0.1333 \ln(\delta/a) - 0.2526 \tag{30}$$

$$t_x^{r*} = t_z^{r*} = 0.4 \ln(\delta/a) - 0.3817 \tag{31}$$

$$f_x^{s*} = f_z^{s*} = 1.701 \tag{32}$$

$$t_x^{s*} = t_z^{s*} = 0.944 \tag{33}$$

In the region $0.01 \leq \delta/a \leq 10$, the following formula can be used to fit the exact solutions tabulated by Goldman *et al.* [51, 48]:

$$\begin{aligned} f_x^{t*} = f_z^{t*} &= -1.388 + 0.2739 \ln \delta/a - 5.216 \times 10^{-2} (\ln \delta/a)^2 \\ &\quad - 2.526 \times 10^{-3} (\ln \delta/a)^3 + 1.709 \times 10^{-4} (\ln \delta/a)^4 \end{aligned} \tag{34}$$

$$\begin{aligned} f_x^{r*} = f_z^{r*} &= 6.837 \times 10^{-3} - 1.638 \times 10^{-2} \ln \delta/a \\ &\quad - 1.123 \times 10^{-2} (\ln \delta/a)^2 \\ &\quad - 1.741 \times 10^{-3} (\ln \delta/a)^3 - 2.662 \times 10^{-4} (\ln \delta/a)^4 \end{aligned} \tag{35}$$

$$t_x^{r*} = t_z^{r*} = -1.045 + 7.832 \times 10^{-2} \ln \delta/a - 3.805 \times 10^{-2} (\ln \delta/a)^2 - 3.603 \times 10^{-3} (\ln \delta/a)^3 + 6.976 \times 10^{-4} (\ln \delta/a)^4 \tag{36}$$

$$f_x^{s*} = f_z^{s*} = 1.701 - \frac{1}{1.423 + 1.287(\delta/a)^{-1.021}} \tag{37}$$

$$t_x^{s*} = t_z^{s*} = 0.994 - \frac{1}{17.45 + 7.012(\delta/a)^{-1.282}} \tag{38}$$

In the region very near the wall for $\delta/a \leq 0.2$, Cox and Brenner [54] suggested that

$$f_y^{t*} = \frac{a}{\delta}\left(1 - \frac{\delta}{5a}\ln\frac{\delta}{a} + 0.9713\frac{\delta}{a}\right) \tag{39}$$

For $0.2 \leq \delta/a \leq 10$, the following fit can be used to the exact solution tabulated by Cox and Brenner [54]:

$$f_y^{t*} = 0.9871 + 1.138\left(\frac{a}{\delta}\right)^{0.9634} \tag{40}$$

Table II summarizes the range of applications of the various expressions for the nonlinear correction and the wall coefficient for the drag force. In the present simulation, the appropriate expressions for the drag force are selected according to this table.

The hydrodynamic drag force acting on a spherical particle attached to a smooth plane surface is given as:

$$F_d = \frac{3\pi f \mu d C_N}{C_c}\sqrt{u_x^2 + u_z^2} \tag{41}$$

TABLE II Regions of validity for various drag nonlinear and wall correction coefficients

Region for C_N	C_N	*Region for wall correction coefficients*	*Wall correction coefficients*
$\mathrm{Re}_p \leq 0.01$	Eq. (24)	$\delta/a \leq 0.01$	Eqs. (29–33), (39)
$0.01 < \mathrm{Re}_p < 20$	Eq. (25)	$0.01 < \delta/a \leq 0.2$	Eqs. (34–38), (39)
$20 \leq \mathrm{Re}_p < 200$	Eq. (22)	$0.2 < \delta/a \leq 10$	Eqs. (34–38), (40)
$\mathrm{Re}_p \geq 200$	Eq. (22)	$\delta/a > 10$	$C_i^w = 1$

where u_x, u_z are, respectively, the streamwise and spanwise components of fluid velocity at the center of sphere, $f(=1.7009)$ is a dimensionless correction factor for the wall effect given by O'Neil [55], and C_N is the nonlinear drag correction given by Eq. (22).

Lift Force

Saffman [56, 57] obtained an expression of lift force for a spherical particle moving in an unbounded shear flow field which is given as

$$\mathbf{F}_L = -\mathrm{sgn}(G)6.46\mu a^2 U_s \left[\frac{|G|}{\nu}\right]^{1/2} \hat{\mathbf{y}} \tag{42}$$

where sgn denotes the signum function, $\hat{\mathbf{y}}$ denotes the unit vector in the direction perpendicular to the wall, $U_s = v_x - u_x$ is the particle-fluid slip velocity, and G is the shear rate defined as

$$G = \frac{du_x}{dy} \tag{43}$$

In his derivation, Saffman assumed that the Reynolds numbers defined in terms of slip velocity, Re_s, and velocity gradient, Re_G, respectively, given by

$$\mathrm{Re}_s = \frac{|U_s|d}{\nu} \tag{44}$$

and

$$\mathrm{Re}_G = \frac{|G|d^2}{\nu} \tag{45}$$

were small compared with unity and satisfy:

$$\mathrm{Re}_s \ll \mathrm{Re}_G^{1/2} \tag{46}$$

However, in a DNS study of aerosol motion in a turbulent channel flow at a moderate Reynolds number, McLaughlin [58] reported that the value of Re_G is typically of the order of 0.04, whereas Re_s is of the order of unity, indicating that Re_s is not small compared with $\mathrm{Re}_G^{1/2}$.

Furthermore, Saffman's formula also is not accurate for predicting the lift force for particles near the wall.

Vasseur and Cox [59] derived the expression for the lift force acting on a sphere moving parallel to a rigid wall through a motionless fluid. Accordingly,

$$\mathbf{F}_L^+ = -\frac{27 U_s^+ G}{8\pi y^{+2} a^+ S |U_s^+ G|} I_u \hat{\mathbf{y}} \tag{47}$$

where superscript '+' denotes nondimensional quantities as defined by Eq. (19), y^+ is the distance from the particle center to the wall, S is the particle-to-fluid density ratio, I_u is an integral, the values of which are tabulated as a function of Re_l in Table III, and Re_l is the Reynolds number based on the distance from the wall defined as

$$\mathrm{Re}_l = |U_s^+| y^+ \tag{48}$$

Asmolov [60] and McLaughlin [58, 61] extended Saffman's work by removing the limitation imposed by Eq. (46). However, the small Reynolds number limitations ($\mathrm{Re}_G, \mathrm{Re}_s \ll 1$) are still required in their analysis. The dimensionless lift force then is given by

$$\mathbf{F}_L^+ = \frac{27 |G^+|^{1/2} U_s^+}{2\pi^2 d^+ S} \frac{G^+}{|G^+|} J \hat{\mathbf{y}} \tag{49}$$

where J is an integral depending on the distance from the wall and the nondimensional parameter given by

$$\varepsilon = \frac{\sqrt{|G^+|}}{U_S^+} \tag{50}$$

TABLE III Values of I_u for various Re_l

Re_l	0.100	0.200	0.300	0.400	0.500	0.600	0.700	0.800	0.900
I_u	0.004	0.016	0.034	0.060	0.092	0.130	0.173	0.220	0.271
Re_l	1.000	1.100	1.200	1.300	1.400	1.500	1.600	1.700	1.800
I_u	0.326	0.383	0.443	0.504	0.566	0.630	0.693	0.757	0.821
Re_l	1.900	2.000	2.500	3.000	3.500	4.000	4.500	5.000	6.000
I_u	0.885	0.948	1.248	1.514	1.741	1.929	2.081	2.203	2.374
Re_l	7.000	8.000	9.000	10.00	20.00	50.00	100.0	200.0	500.0
I_u	2.475	2.532	2.561	2.572	2.423	2.050	1.832	1.705	1.617

McLaughlin [61] tabulated the values of J as a function of y^+ and ε which are reproduced in the Tables IV and V.

Cox and Hsu [62] gave an expression for the lift force when the wall lies in the inner region of the particle disturbance flow, and this equation is applied in the region $a \ll y \ll \min(L_G, L_S)$. Here, L_G and L_S are called the Saffman length and the Stokes length, respectively, defined as

$$L_G = \left(\frac{\nu}{|G|}\right)^{1/2} \tag{51}$$

TABLE IV Values of J for positive ε

y^+	$\varepsilon = 0.2$	0.4	0.6	0.8	1.0	1.5	2.0	∞
0.1	3.07	1.65	1.14	0.881	0.720	0.505	0.409	0.143
0.2	2.82	1.69	1.23	0.982	0.826	0.615	0.521	0.255
0.4	2.06	1.56	1.25	1.07	0.943	0.766	0.686	0.455
0.6	1.52	1.42	1.25	1.12	1.03	0.891	0.827	0.631
0.8	1.16	1.30	1.23	1.15	1.09	0.983	0.934	0.771
1.0	0.903	1.19	1.20	1.17	1.13	1.05	1.01	0.886
1.2	0.727	1.08	1.17	1.18	1.16	1.12	1.10	1.01
1.4	0.580	0.977	1.12	1.17	1.18	1.17	1.17	1.12
1.6	0.475	0.889	1.08	1.16	1.19	1.21	1.23	1.22
1.8	0.398	0.816	1.04	1.15	1.20	1.25	1.52	1.30
2.0	0.342	0.766	1.01	1.14	1.21	1.28	1.69	1.37
3.0	0.192	0.572	0.908	1.13	1.27	1.44	1.52	1.69
4.0	0.126	0.463	0.857	1.15	1.34	1.58	1.69	1.89
5.0	0.090	0.396	0.848	1.19	1.42	1.70	1.82	2.02
∞	−0.0125	0.408	1.024	1.436	1.686	1.979	2.094	2.255

TABLE V Values of J for negative ε

y^+	$\varepsilon = -0.2$	−0.4	−0.6	−0.8	−1.0	−1.5	−2.0	$-\infty$
0.1	−2.90	−1.46	−0.952	−0.695	−0.542	−0.338	−0.223	0.143
0.2	−2.55	−1.34	−0.844	−0.589	−0.435	−0.230	−0.114	0.255
0.4	−1.68	−0.980	−0.566	−0.334	−0.191	0.001	0.110	0.455
0.6	−1.11	−0.704	−0.340	−0.119	0.018	0.204	0.308	0.631
0.8	−0.745	−0.492	−0.157	0.057	0.191	0.371	0.471	0.771
1.0	−0.504	−0.317	0.0015	0.211	0.342	0.515	0.610	0.886
1.2	−0.358	−0.178	0.146	0.362	0.495	0.666	0.757	1.01
1.4	−0.239	−0.048	0.287	0.508	0.642	0.809	0.896	1.12
1.6	−0.162	0.051	0.404	0.634	0.771	0.937	1.02	1.22
1.8	−0.111	0.126	0.501	0.743	0.884	1.05	1.13	1.30
2.0	−0.076	0.182	0.576	0.827	0.972	1.14	1.22	1.37
3.0	−0.016	0.314	0.805	1.12	1.30	1.51	1.59	1.69
4.0	−0.003	0.354	0.898	1.25	1.46	1.70	1.80	1.89
5.0	−0.0007	0.370	0.939	1.32	1.54	1.81	1.91	2.02
∞	−0.0125	0.408	1.024	1.436	1.686	1.979	2.094	2.255

$$L_S = \frac{\nu}{|U_s|} \tag{52}$$

Cherukat and McLaughlin [63] extended Cox and Hsu's work by removing the limitation, $y \gg a$. The corresponding dimensionless lift force then is given as:

$$\mathbf{F}_L^+ = \frac{3U_s^2 G}{4\pi a^+ S|G|} I\hat{\mathbf{y}} \tag{53}$$

where I is a dimensionless factor depending on the distance of the particle from the wall, the shear rate and the particle size. For a freely-rotating sphere in the near-wall region, I is given as:

$$\begin{aligned} I = {} & (1.7631 + 0.3561\kappa - 1.1837\kappa^2 + 0.8452\kappa^3) \\ & - (3.2414/\kappa + 2.676 + 0.8248\kappa - 0.4616\kappa^2)\Lambda_G \quad \text{for } U_S^+ \neq 0 \\ & + (1.8081 + 0.8796\kappa - 1.9009\kappa^2 + 0.9815\kappa^3)\Lambda_G^2 \\ I = {} & 336\pi/576 \quad \text{for } U_S^+ = 0 \end{aligned} \tag{54}$$

In this equation, the nondimensional parameters, κ and Λ_G, are defined as

$$\kappa = \frac{a}{y} \tag{55}$$

$$\Lambda_G = -\frac{Ga}{U_s} \tag{56}$$

Table VI summarizes the validity regions of various expressions for the lift force. In the present simulation, appropriate expressions for the lift force are selected according to this table.

TABLE VI Regions of validity for various lift force expressions

	$\lvert\varepsilon\rvert < 0.2$	$\lvert\varepsilon\rvert \geq 0.2$
$y^+ < 0.1$	Eq. (53)	Eq. (53)
$0.1 \leq y^+ \leq 5$	Eq. (47)	Eq. (49)
$y^+ > 5$	Eq. (42)	Eq. (49)

Leighton *et al.* [64] derived an expression for the lift force for a sphere attached to a wall in a linear shear flow, given as:

$$\mathbf{F}_L^+ = \frac{6.915 U_s^2 G}{\pi a^+ S|G|}\hat{\mathbf{y}} \tag{57}$$

Cherukat and McLaughlin [63] showed that the integral given by Eq. (54) tends to $I = 9.22$ as $y/a \rightarrow 1$ which is compatible with Eq. (57) of Leighton *et al.* [64]. Therefore, Eq. (57) is applied for evaluating the lift force for a spherical particle attached to a surface.

Hydrodynamic Torque

For a sphere in contact with a plane surface, the hydrodynamic torque acting on the particle is given by

$$M_t = 2\pi\mu C_M d^2 \sqrt{u_x^2 + u_z^2} \tag{58}$$

where $C_M = 0.943993$ is the correction factor for the wall effects as derived by O'Neill [55].

Brownian Force

The nondimensional Brownian force is given as (Ounis *et al.* [38, 39]);

$$n_i^+(t^+) = \frac{6\nu}{\pi \rho^p d^3 u^{*3}} N_i(t^+) \tag{59}$$

The spectral intensity of n_i^+ was given by Ounis *et al.* [38, 39], *i.e.*,

$$S_{n_i^+ n_j^+}(\omega^+) = \frac{648}{\pi C_c^2} \frac{\delta_{ij}}{S_c S^2 d^{+4}} = \frac{2}{\pi S_c \tau_p^{+2}} \delta_{ij} \tag{60}$$

where

$$S_c = \frac{\nu}{D} = \frac{3\pi\nu d\mu}{C_c k T} \tag{61}$$

is the Schmidt number, ω^+ is the frequency in wall units, T is the air temperature, μ is the air viscosity, $k = 1.38 \times 10^{-23}$ J/K is the

Boltzmann constant, and D is the particle Brownian diffusivity. In Eq. (60) τ_p^+ is the nondimensional particle relaxation time. The dimensional and nondimensional particle relaxation time are given as:

$$\tau_p = \frac{C_c S d^2}{18\nu}, \quad \tau_p^+ = \frac{C_c S d^{+2}}{18} \tag{62}$$

The Stokes–Cunningham slip correction factor, C_c, is given by Eq. (21). At every time step in a simulation, the dimensionless Brownian force is given as:

$$n_i^+(t^+) = G_i \sqrt{\frac{\pi S_0}{\Delta t^+}} \tag{63}$$

where G_i is a zero-mean independent Gaussian random number, S_0 is the spectral intensity, and Δt^+ is the time increment.

RESULTS AND DISCUSSION

In this section, particle removal, resuspension and re-entrainment in the turbulent channel flows are studied. A temperature of $T = 298$ K, a kinematic viscosity of $\nu = 1.5 \times 10^{-5}\,\mathrm{m^2/s}$, and a density of $\rho^f = 1.12\,\mathrm{kg/m^3}$ for air, a density ratio of $S = 1964$ for graphite particle, and a shear velocity of $u^* = 1.0\,\mathrm{m/s}$ are assumed. In this case, the Reynolds number based on the shear velocity, u^*, and the half-channel width is 125, while the flow Reynolds number based on the hydraulic diameter and the centerline velocity is about 8000. This condition corresponds to a channel width of 3.75 mm. To keep the computational effort within an acceptable limit and to reduce the statistical error, ensembles of 8192 (2^{13}) particles for each diameter are used in these simulations. The gravity is assumed to be in the direction perpendicular to the lower wall.

REMOVAL AND ADHESION

In this section, ensembles of different size particles are initially randomly distributed on the lower wall, and all forces acting on each particle are computed at every time step. When the detachment condition (Eqs. (15) or (16)) is satisfied, the particle is assumed to be resuspended in the turbulent flow, and its subsequent motion is simulated using Eqs. (17) and (18).

Figure 3a shows variations of the number of removed 40 and 50 μm graphite particles *versus* time as predicted by the JKR and the TPL adhesion models. It is observed that the number of particles removed as predicted by the JKR model is larger than that obtained from the TPL model. This trend is consistent with the earlier results reported by Soltani and Ahmadi [17]. Since the JKR model has been more accepted in the literature, it is used in the following simulations for particle removal from surfaces.

Variations of the number of particles that are resuspended and those that remain attached or redeposit on the lower wall as a function of time are shown in Figure 3b. This figure shows that the number of resuspended particles increases up to about $t^+ = 400$ and then

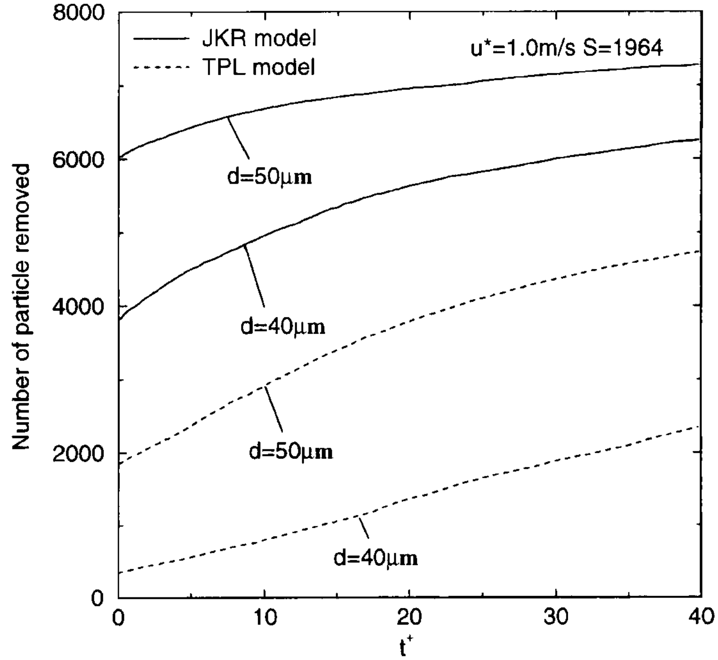

FIGURE 3a Variations of the number of removed particles *versus* time for different adhesion models.

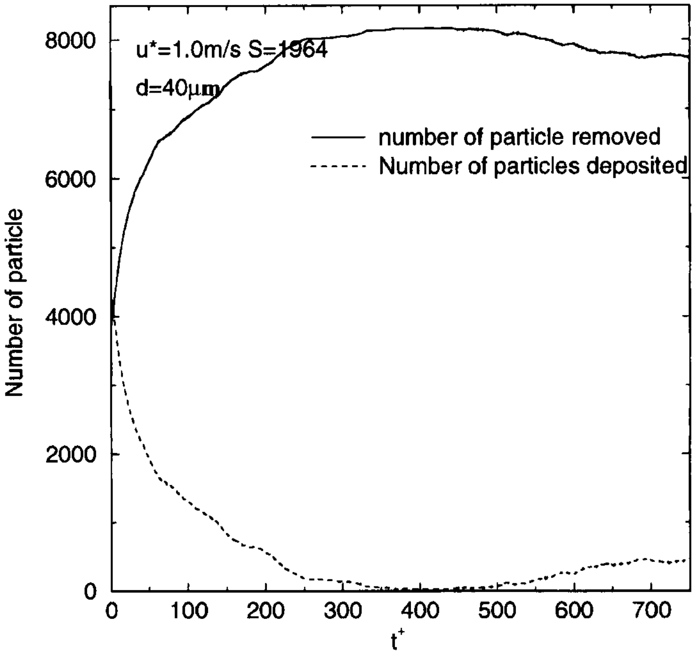

FIGURE 3b Variations of the number of removed and deposited particles *versus* time.

equilibrates at about 7700. At the equilibrium condition, about 95% of particles are resuspended. For $t^+ < 400$, the particle resuspension process is dominant; but, for $t^+ > 400$, the resuspension and deposition processes tend to come to equilibrium. The simulation was repeated for 40 μm glass, polystyrene, silicon and rubber particles. Figure 3c shows the number of removed particles *versus* time for different materials. It is observed that graphite, glass, polystyrene and silicon particles are more easily removed when compared with rubber particles. This is because the softer rubber particles form a larger contact area and have a higher adhesion force.

Particle Detachment Mechanism

In this section, the statistical properties of various nondimensional forces and moments acting on the particles attached to the lower wall of the channel are evaluated at every time step, and their variations are discussed. The results for an ensemble of 8192 graphite particles with a

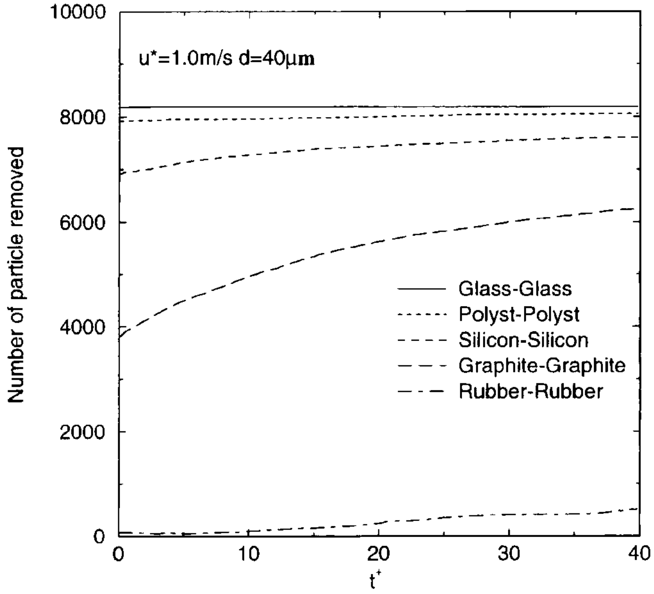

FIGURE 3c Variations of the number of removed particles *versus* time for different materials.

diameter of $d = 40\,\mu\mathrm{m}$ ($\tau_p^+ = 780$) are described. It is found that all particles detach from the wall by the rolling detachment mechanism. This is consistent with the suggestion of Soltani and Ahmadi [17] that the rolling detachment is the dominant resuspension mechanism of spherical particles in turbulent flows.

Figure 4a shows the probability density function of dimensionless drag and hydrodynamic torque for particles that are removed and the particles that remain attached to the wall. The statistical results are obtained in the time period (0, 40) in wall units. The density function is evaluated using $f(\xi) = N_\xi/N$, where N_ξ is the number of particles with the nondimensional drag force in the region $[\xi, \xi + \Delta\xi]$, and N is the total number in the sample. Here, $\Delta\xi = 1.0 \times 10^{-4}$ is assumed, and the density function satisfies the normalization condition, $\sum_{i=1}^{200} f(\xi_i) = 1$, where 200 is the number of bins used in the analysis. It is observed that there exists a threshold value of about 0.003 for the drag force for the removed particles. Particles will detach from the wall when the drag force is beyond the threshold value. Figure 4a also shows that the dimensionless drag force for particles that remain attached to the wall

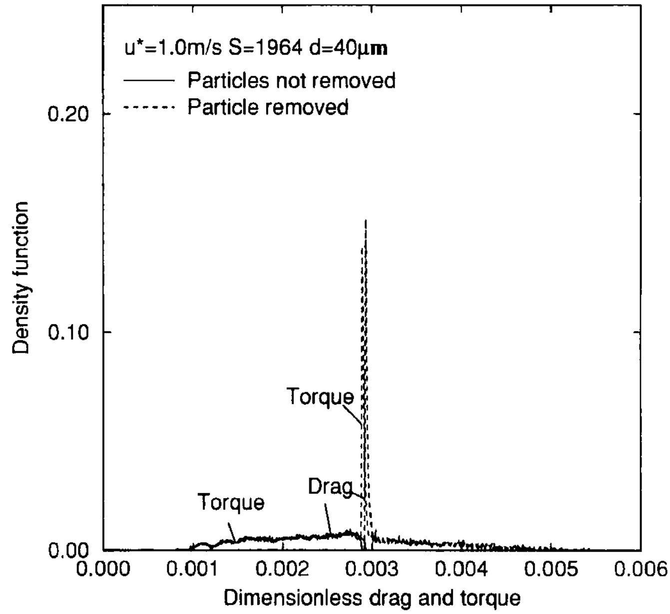

FIGURE 4a Probability density function of dimensionless drag and torque for removed and deposited particles.

is distributed roughly uniformly between 0.001 and 0.003, while the density function of drag force for removed particles has a high peak which is slightly larger than the threshold value. This indicates that most detachment occurs when the drag force begins to exceed the threshold value. Figure 4a also shows that the density function of torque is similar to that of the drag force and the threshold value of torque is slightly smaller than that for the drag force. Similar probability density functions for the lift force are shown in Figure 4b. While there is an approximate critical value of 0.0004 for the nondimensional lift force, there is a noticeable spread in the distributions, and the density functions of the lift force for particles removed and attached overlap. This indicates that the lift force is not the critical factor for particle detachment.

The mean values of nondimensional forces and hydrodynamic torque acting on the removed and attached 40 μm particles are shown in Table VII. The mean value of adhesion force is at least three orders of magnitude larger than those of the gravitational and lift forces.

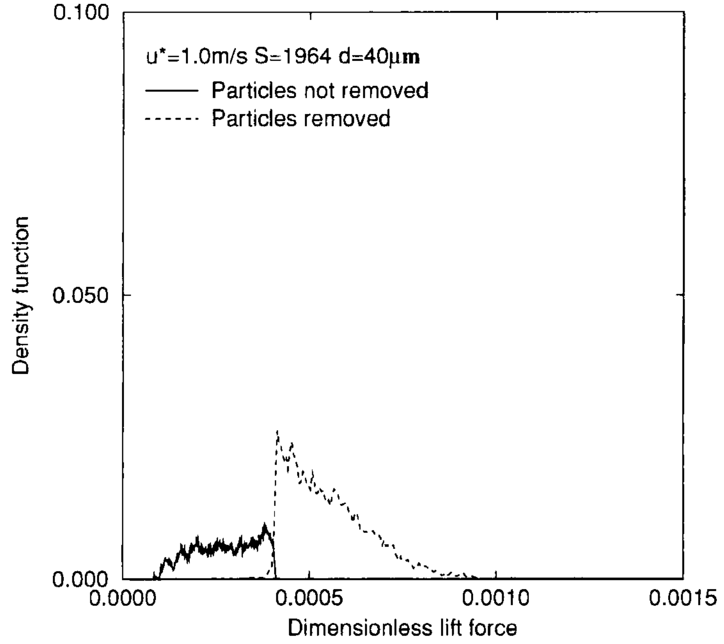

FIGURE 4b Probability density function of dimensionless lift force for removed and deposited particles.

TABLE VII Mean values of various forces and moments for $d = 40\,\mu m$ graphite particles

	Lift force	*Gravity*	*Adhesion force*	*Drag*	*Moment*
Removed particle	5.50e-4	1.47e-4	1.49	3.48e-3	3.34e-3
Attached particle	2.72e-4	1.47e-4	1.49	2.11e-3	2.08e-3

Therefore, the effects of gravity and lift force for particle (lift-off) detachment are negligible. The magnitudes of drag force and hydrodynamic torque are comparable and, thus, they both play an important role in the particle rolling detachment process. (Note that here $d^+ = 2.67$ for 40 μm particles.)

Turbulent Near Wall Structure

Hinze [19] and Smith and Schwartz [65] summarized the streaky structures of turbulent near-wall flows. In the earlier works of Ounis *et al.* [39], Soltani and Ahmadi [36] and Zhang and Ahmadi [47], it was shown that the turbulence near-wall coherent eddies play a dominant role in particle deposition and resuspension processes. We performed several simulations with ensembles of 8192 particles of different sizes (from 30 µm to 60 µm) that are initially uniformly distributed on the lower surface of the duct. Figure 5 shows the locations of particles that remained attached on the lower wall at $t^+ = 40$. For 30 µm particles, Figure 5a shows that the particles are removed in certain bands. The attached particles also form roughly distinct bands. Similar trends are also observed in Figure 5b for 40 µm particles. Here, the structure of bands is more pronounced. In this figure, the distances between the nearby bands are about 100 – 150 wall units, which is consistent with spacing between high-speed and low-speed streaks as was also noted by Soltani and Ahmadi [42]. Similar band structures also exist for particles with $d = 50$ µm and $d = 60$ µm as shown in Figures 5c and 5d. The number of particles that remain attached to the wall, however, decreases rapidly as particle diameter

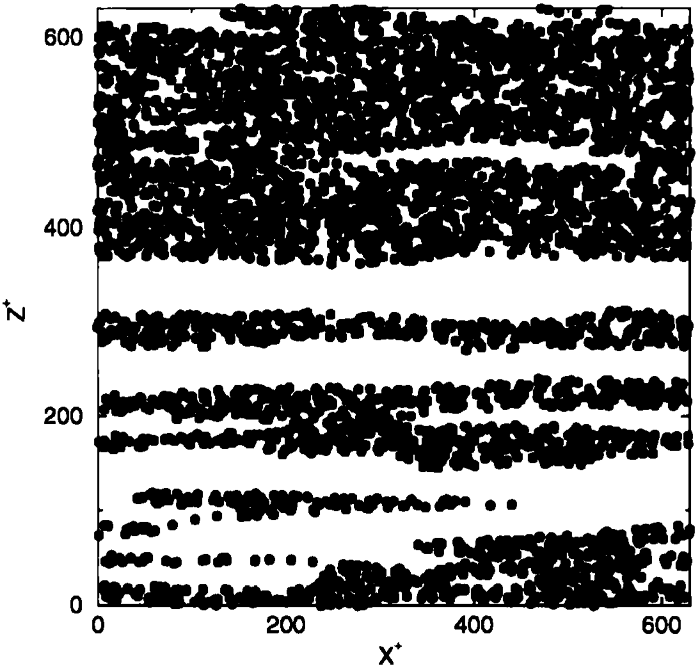

FIGURE 5a Distribution of the locations of 30 µm particles on the surface.

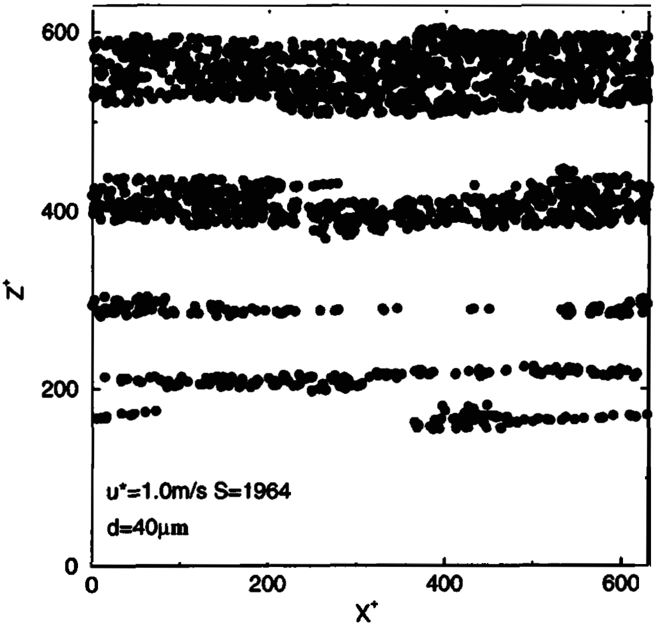

FIGURE 5b Distribution of the locations of 40 μm particles on the surface.

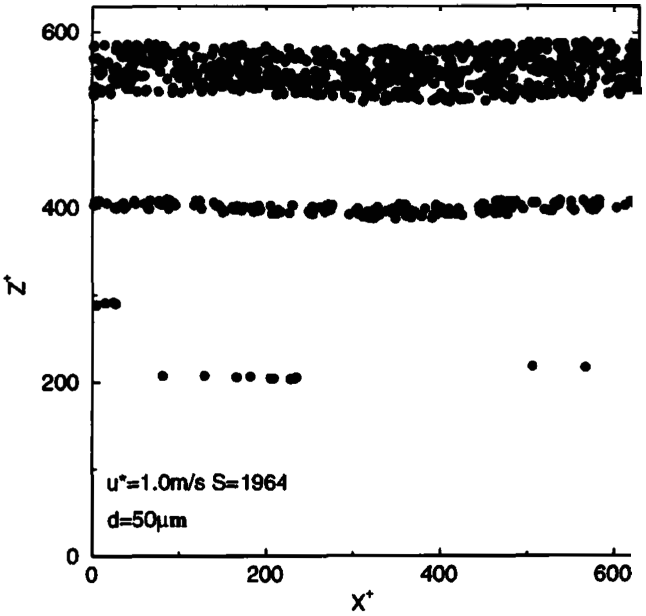

FIGURE 5c Distribution of the locations of 50 μm particles on the surface.

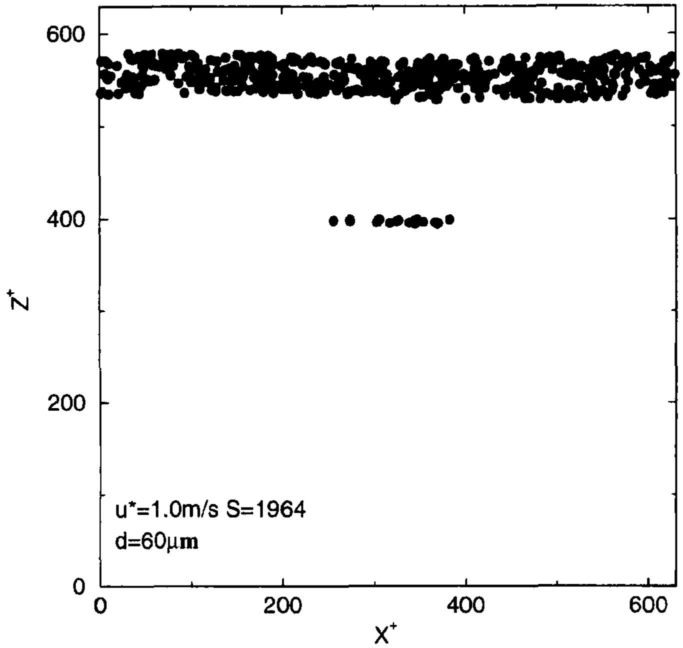

FIGURE 5d Distribution of the locations of 60 μm particles on the surface.

increases. This is because the hydrodynamic forces and torques acting on the particles increase faster than the adhesion force as *d* increases, while the effect of weight is negligible. Figure 5 further confirms the importance of near-flow structure (coherent vortices, high- and low-speed streaks) in particle removal and re-entrainment processes in turbulent flows.

Variations of mean velocity components averaged spatially over one periodic cycle in the streamwise direction at a distance of 1.33 wall units from the lower wall (corresponding to the centroid of a 40 μm particle) and temporally in a time period of (0, 40) wall units are shown in Figure 6a. It is observed that the streamwise velocity varies between 0.5 to 2.2 with a mean value of about 1.3. Both u^+ and w^+ components exhibit roughly periodical fluctuations in the spanwise direction. The amplitude of the streamwise velocity fluctuation is about 0.6 while that of w^+ varies between 0.1 to 0.3. This observation is consistent with the well-known streaky structure of turbulence in the near-wall region. Figure 6a shows that the peaks and valleys of u are

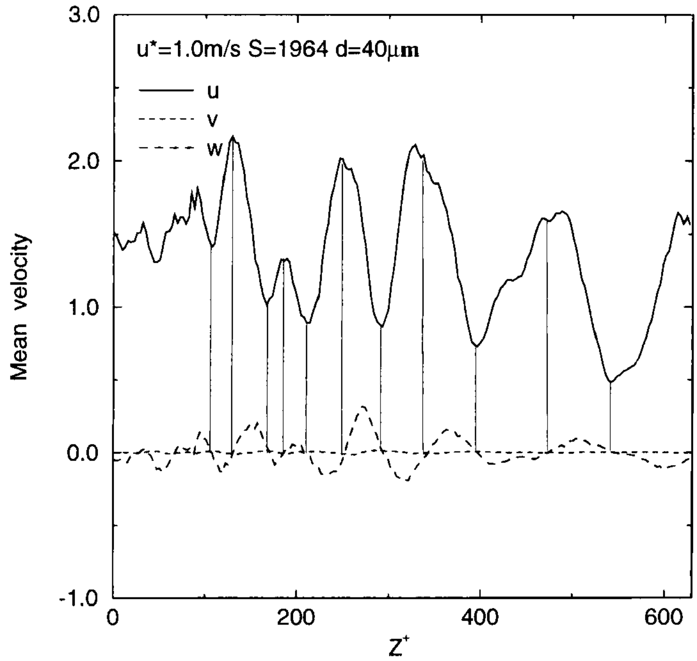

FIGURE 6a Spanwise variation of the averaged nondimensional velocities.

roughly at the points that w^+ becomes zero. The mean normal velocity is comparatively quite small. The periodic (positive and negative) variation of w^+ clearly indicates the presence of counter-rotating near-wall vorticies in the average sense. Figure 6b shows the close up of the v^+-velocity. The nearly-periodic fluctuation structure of v^+ is clearly observed from this figure. Comparing the locations of the peaks and valleys of the averaged velocity components in these figures shows that the high-speed streaks (peaks of u^+) correspond to the down-flow region (v^+ toward the wall). Similarly, the low-speed streaks correspond to upflow regions. This result is consistent with the early observation of periodic averaged vorticity reported by Soltani and Ahmadi [42].

Table VII showed that the hydrodynamic drag and torque acting on particles are the dominant factors for particle detachment. The magnitudes of hydrodynamic drag and torque are directly proportional to the particle-fluid slip velocity as indicated by Eqs. (41) and

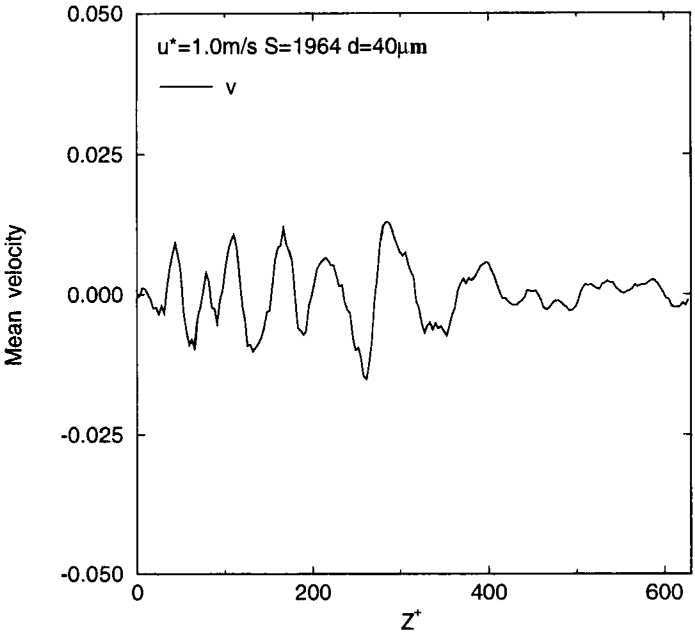

FIGURE 6b The close up of the spanwise variation of v-velocity.

(58). The magnitude of the streamwise velocity is much larger than the spanwise component. Thus, the streamwise velocity is the key parameter for particle removal from the wall. A careful examination of the result reveals that the bands in Figure 5 for which the particles are removed coincide with the regions in which u^+ is near its peaks in Figure 6. These observations show that the turbulence near-wall structures play an important role on the particle removal process.

Removal Rate

Reeks *et al.* [30] proposed a model for particle removal based on the influence of turbulence fluctuation energy transferred to particles attached to the wall. They found two distinctive regimes: an "initial" resuspension region in which about 90% of the particles are removed during a short initial burst lasting typically less than 10^{-2} s, which is followed by a "longer-term" gradual resuspension at a rate inversely proportional to time. The resuspension rate obtained in our simulations for 40 μm and 50 μm particles are shown in Figure 7. The

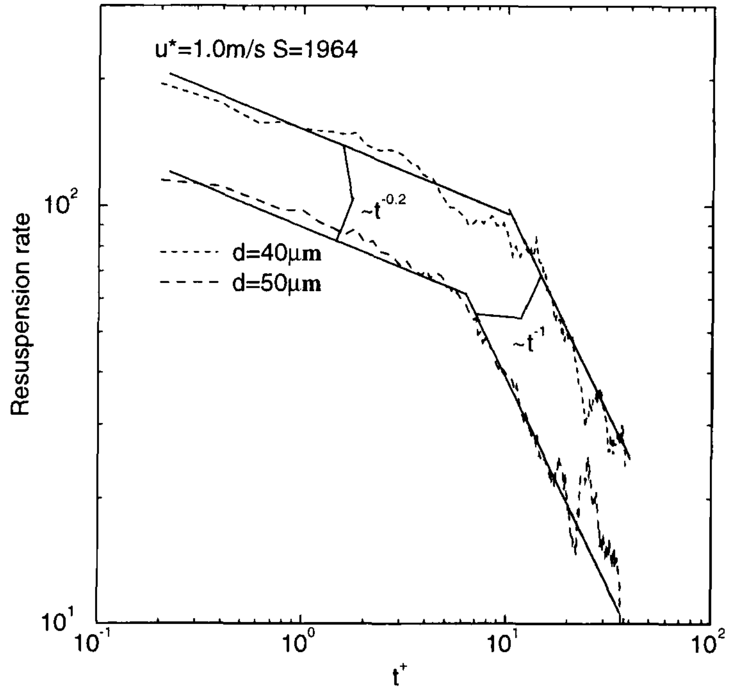

FIGURE 7 Variations of the resuspension rate *versus* time.

resuspension rate is defined as

$$\Lambda(t^+) = \frac{\Delta N}{\Delta t^+} \tag{64}$$

where ΔN is the number of particles resuspended in a time interval of Δt^+. Figure 7 shows a decreasing removal rate as the particle concentration on the wall is depleted. The trend in the variation of Λ, however, markedly changes. For 50 μm particles, when $t^+ < 5$, Λ varies as $t^{-0.2}$; while, for $t^+ > 7$, the removal rate varies roughly as t^{-1}. For 40 μm particles, similar trends in the variation are seen, but the change in slope occurs at $t^+ \approx 12$. The dimensional time duration used for evaluating the resuspension rate in these simulations is of the order of 10^{-3} s, which corresponds to the initial resuspension region suggested by Reeks *et al.* [30]. There are no experimental data available for such a short time duration, and the results can only be compared with the trend of Reeks' resuspension model which is in qualitative agreement with the field observation. Figure 7 shows that the variation of resuspension rate with time is comparable with the model of Reeks *et al.* [30]. The simulated "long-term" t^{-1} variations of resuspension rate, however, seem to initiate at a much short time when compared with the model.

RE-ENTRAINMENT TRAJECTORIES

In this section, ensembles of particle trajectories which are removed from the wall are computed and statistically analyzed. Here, a particle-to-fluid density ratio of $S=1964$ and a shear velocity of $u^*=1.0\,\mathrm{m/s}$ are assumed.

Re-entrainment Process

As noted before, an ensemble of 8192 particles with $d=40\,\mu\mathrm{m}$ are initially randomly distributed on the lower wall. The particles are assumed to be resuspended when the detachment condition given by Eq. (15) is satisfied. The subsequent trajectories of detached particles are then evaluated using Eq. (17). In this case, $\tau_p=0.012\,\mathrm{sec}$ and $\tau_p^+=780$. Figure 8 shows the instantaneous locations of particles in the $y-z$ plane at different times. For $t^+=250$, it is observed from Figure 8a that particles begin to move away from the wall. Their transport, however, is not a uniform diffusion process and shows definite structures in the spanwise direction. Figure 8b shows instantaneous particle locations at $t^+=500$. The periodic spanwise structure can clearly be seen from this figure. The instantaneous particle locations at $t^+=750$ and $t^+=1000$ are shown in Figures 8c and 8d, respectively. Figure 8c shows that particles seem to move away from the wall on certain distinct bands. While the bands are also noticeable in Figure 8d, the structure tends to smear out due to the movements of the near wall coherent eddies and turbulence dispersion in the core region.

Sample trajectories in different planes are shown in Figure 9. Trajectories in the $y-z$ plane in Figure 9a indicate that $40\,\mu\mathrm{m}$ particles first move away from the wall roughly straight up to about 7 to 10 wall

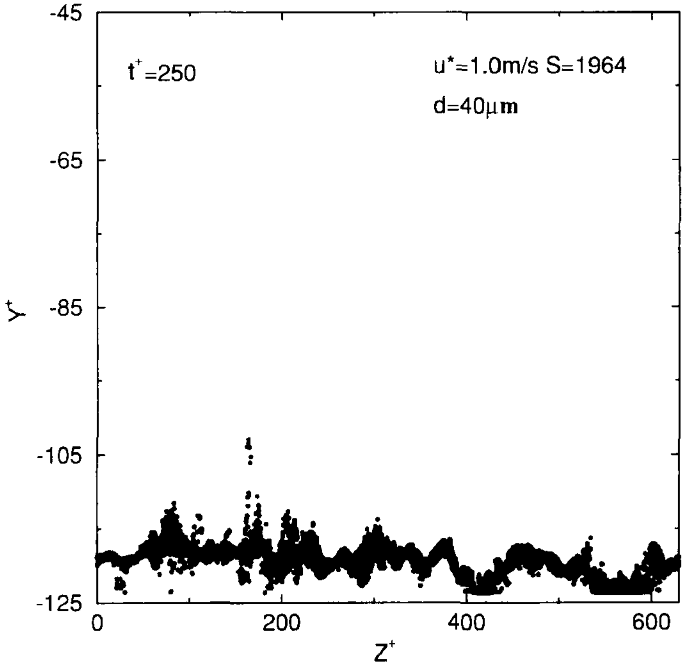

FIGURE 8a Distribution of 40 μm particles in the $y-z$ plane at $t^+ = 250$.

units from the wall and then begin to disperse. Figure 9b shows the close up of a few particle trajectories in the $y-z$ plane. Particle removal, deposition, and resuspension processes are seen from this figure. The roughly straight upward motion of detached particles is also clearly noticeable. Figure 9c shows the $x-y$ projection of 40 μm particle trajectories that are initially on the wall on a line at about $x^+ = 500$. It is observed that some particles are swept away by the streamwise fluid velocity and are entrained in the core flow. A number of removed particles deposit on the wall and are resuspended again. Figure 9d shows that 40 μm particles move in the streamwise direction and away from the wall roughly in their vertical planes with little dispersion in wall region, but disperse as they enter the core flow region. The simulation results presented in Figures 8 and 9 suggest that streaky axial flow structure together with the lift force play a key role in the detachment of particles larger than 40 μm and their reentrainment processes from the wall region.

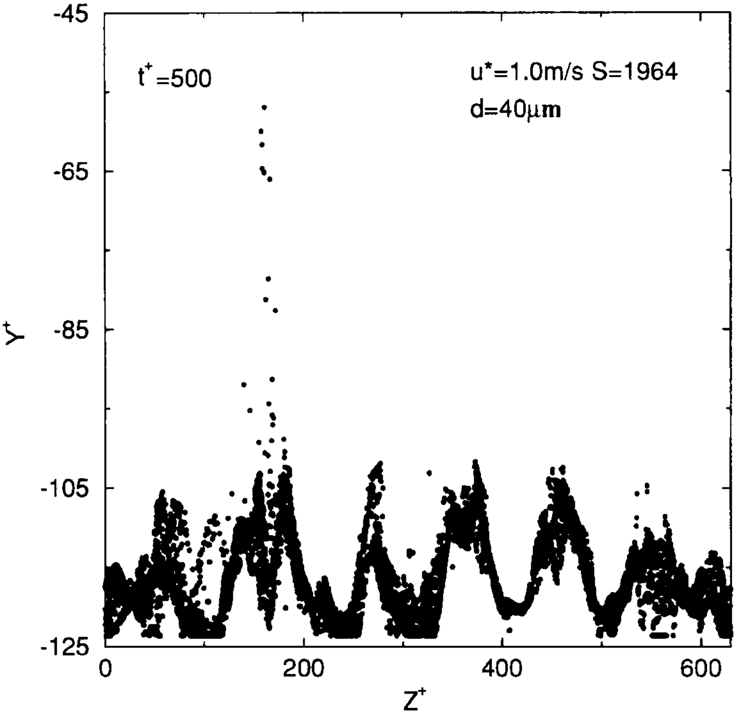

FIGURE 8b Distribution of 40 μm particles in the $y-z$ plane at $t^+ = 500$.

To analyze the re-entrainment process for sub-micrometer particles, the simulation is repeated for an ensemble of 8192 particles with $d = 0.14\,\mu m$. In this case, $\tau_p = 3.4 \times 10^{-7}$ sec and $\tau_p^+ = 0.023$. The particles are initially randomly distributed at a distance of one wall unit from the lower wall, and their subsequent trajectories are analyzed. Figure 10 shows particle positions in the $y-z$ plane at different times. Figure 10a indicates that the 0.14 μm particle concentration in the $y-z$ plane is nonuniform, and the particles tend to move away from the wall in certain bands. Similar structures in the distribution of particles are also noticeable at $t^+ = 500$, 750, 1000 shown in Figures 10b–10d. These small particles, however, exhibit more dispersion due to the Brownian motion effects.

Figures 11a–11c show sample particle trajectories for $d = 0.14\,\mu m$ in different planes in a time duration of (0, 1000) wall units. Contrary to the large 40 μm particles, these small particles do not move straight up,

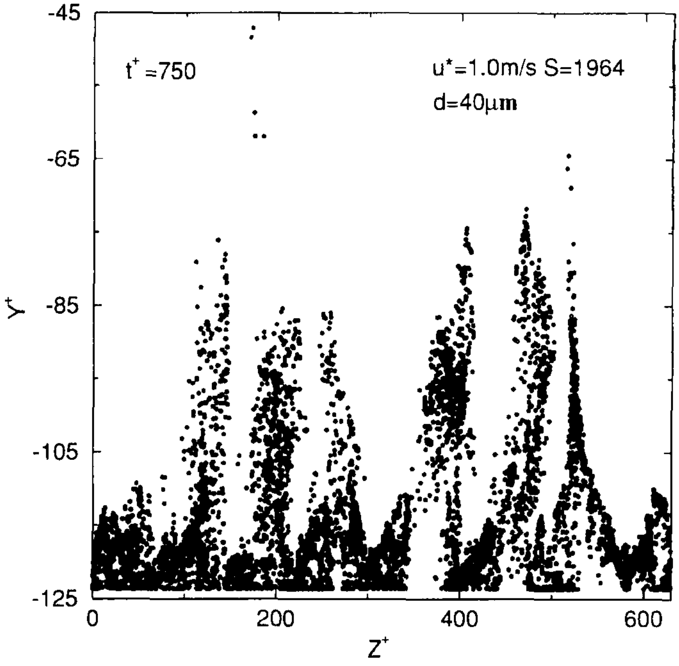

FIGURE 8c Distribution of 40 μm particles in the $y-z$ plane at $t^+ = 750$.

and their trajectories in the $y-z$ plane are curved and roughly follow the coherent near-wall vortices. Figure 11b shows that the resuspended 0.14 μm particles are, generally, dispersed in the flow with little re-deposition. Random trajectories of these particles (due to turbulence and Brownian motion) are clearly seen from Figures 11a–11c.

To clarify further the effect of near-wall turbulence structure on the particle re-entrainment process, the statistics of the simulated fluid velocity components near the wall are obtained. Averaging is performed spatially along the streamwise direction and temporally in a time period of (0, 100). Figure 12a shows the contours of the mean u^+-velocity in the $y-z$ plane. The periodic pairing of high-speed and low-speed streaks near the wall are clearly seen from this figure. The similar result for the v^+-velocity shown in Figure 12b indicates the periodic upward and downward flow structures. Comparing Figure 12a and 12b, it is found that the locations of the high-speed axial flow stream ($z^+ = 40$, 140, 260, 350, 480, 600) correspond to those of

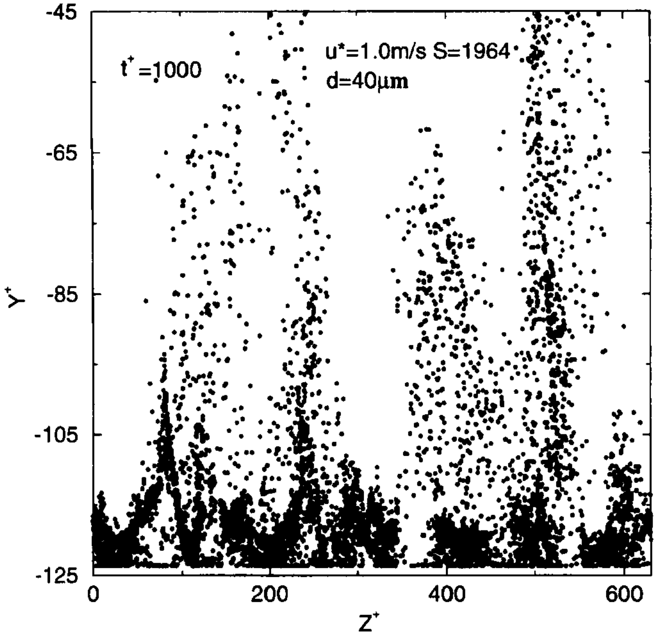

FIGURE 8d Distribution of 40 μm particles in the $y-z$ plane at $t^+ = 1000$.

downward flows (negative v^+); and the locations of the low-speed stream ($z^+ = 80, 200, 300, 400, 550$) correspond to those of upward flows.

The formation of U-shaped vortex loops, also known as horseshoe or hairpin vortices, is one important feature of turbulent boundary-layer flow in the models of Acarlar and Smith [66] and Robinson [67]. In this model, vortices play a major role in producing sweeps and ejections in the near-wall shear layers. A careful examination of the results shows that the locations of peaks of concentration of 40 μm particles in Figure 8b roughly correspond to those of high-speed axial streams in Figure 12a and downward flow regions in Figure 12b. In contrast, the peaks in the distribution of 0.14 μm particles shown in Figures 10a and 10b correspond to the upward flow regions in Figure 12b (and low u^+ in Fig. 12a). That is, the re-entrainment of large and small particles is controlled by different mechanisms. Large particles with $d = 40$ μm ($\tau_p^+ = 780$) move roughly straight from the wall up to about 10 wall units due to the shear-induced lift force, then begin to disperse. As a result, these particles move away faster from the wall in

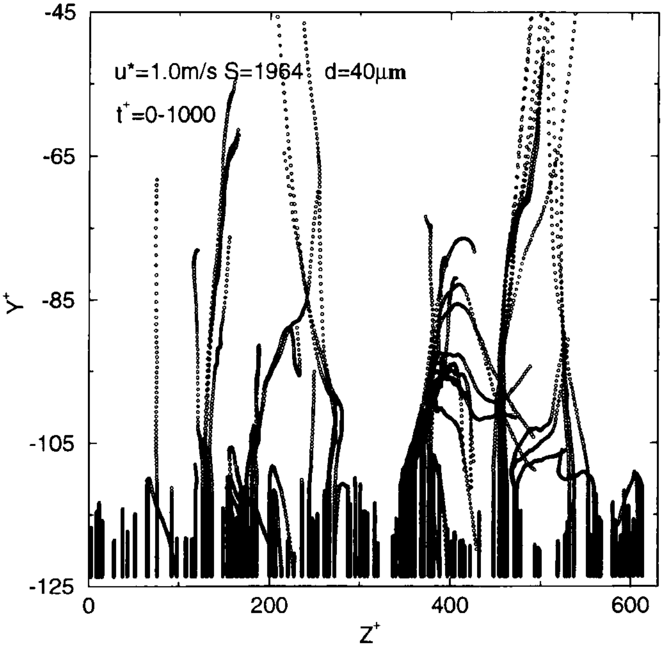

FIGURE 9a Sample 40 μm particle trajectories in the $y-z$ plane.

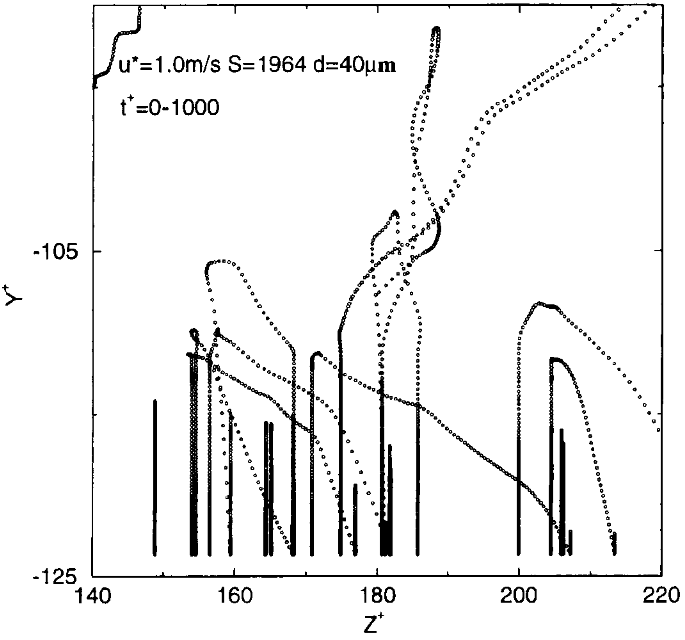

FIGURE 9b Close up of 40 μm particle trajectories in the $y-z$ plane.

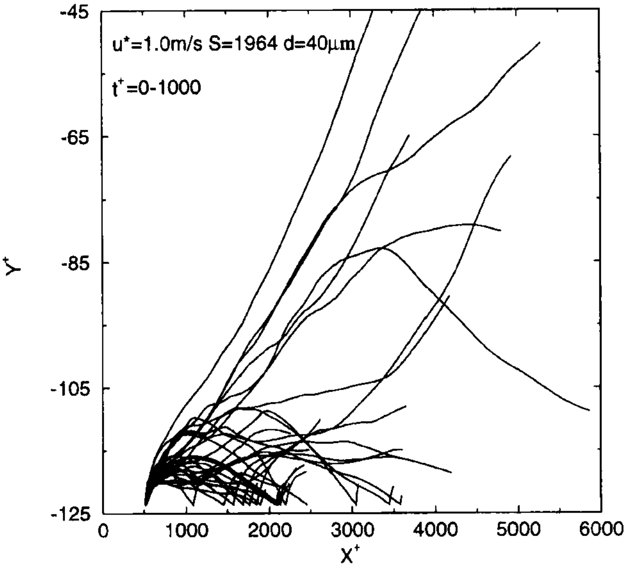

FIGURE 9c Sample 40 μm particle trajectories in the $x-y$ plane.

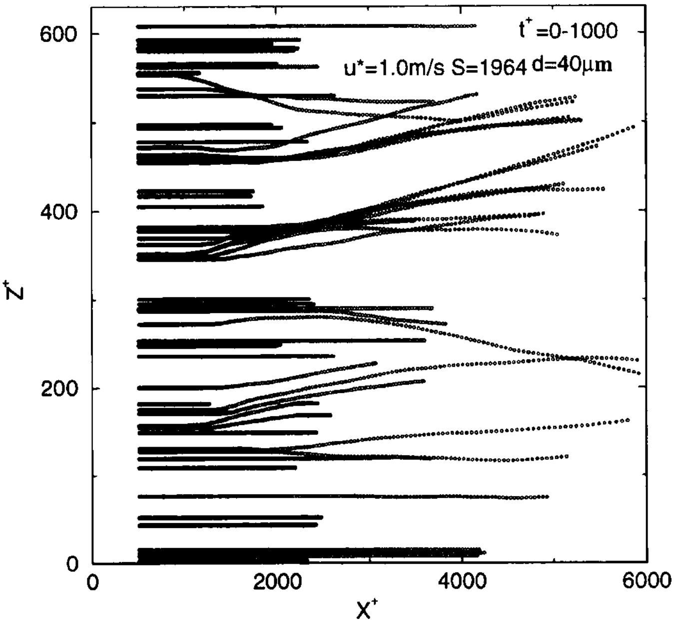

FIGURE 9d Sample 40 μm particle trajectories in the $x-z$ plane.

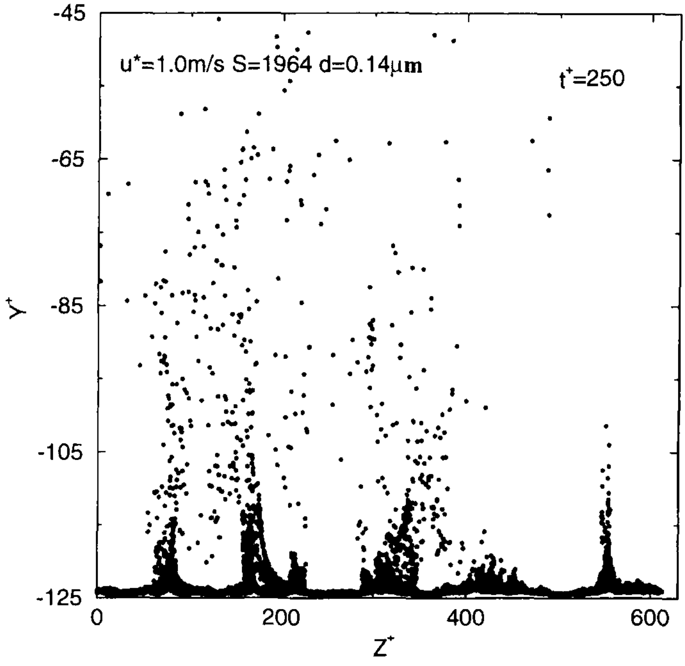

FIGURE 10a Distribution of 0.14 μm particles in the $y-z$ plane at $t^+ = 250$.

the high streamwise velocity bands, which correspond to downward flow regions (negative v^+). The small particles of the order of 0.1 μm ($\tau_p^+ = 0.023$), however, follow the near-wall upward flows formed by the near-wall coherent eddies. These regions correspond to the low streamwise velocities.

To the authors' knowledge there is no experimental data that could provide insight in the micro-mechanics of the particle removal process. The difficulty is the time scale of the dynamic rearrangement of the near-wall eddies, which is quite small compared with the macroscopic time, but sufficiently large compared with the time scale of particle removal from the wall region.

Plane Source

Additional simulations are performed to provide further understanding of the particle re-entrainment process. An ensemble of 8192

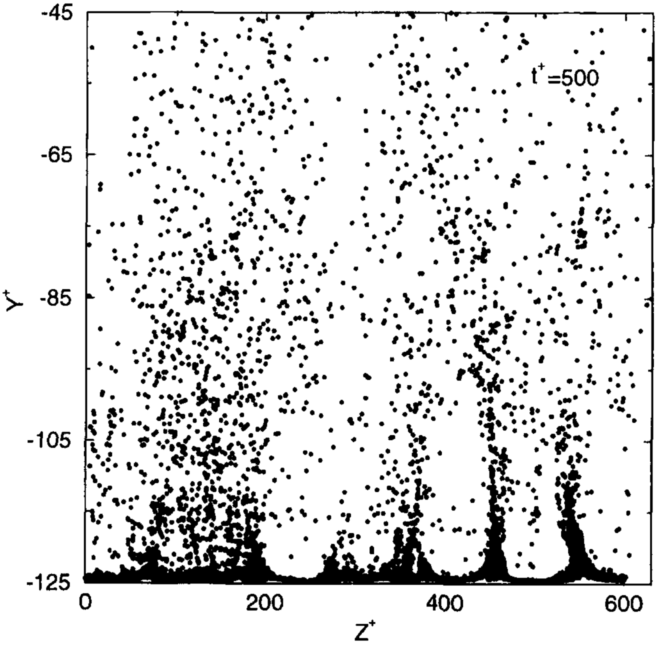

FIGURE 10b Distribution of 0.14 μm particles in the y–z plane at $t^+ = 500$.

particles with $d = 0.14\,\mu\text{m}$ ($\tau_p^+ = 0.023$) and $d = 40\,\mu\text{m}$ ($\tau_p^+ = 780$) are initially released randomly in a plane at a distance of 1.5 wall units from the lower wall in a horizontal duct. At every time step, the particle positions are evaluated and statistically analyzed. The mean, the maximum, the minimum and the mean standard deviation (mean $\pm\,\sigma$) trajectories are computed; and the results are displayed in Figure 13. The mean paths for 0.14 μm and 40 μm particles are very close, while 0.14 μm particles disperse away from the wall much faster than 40 μm particles. Therefore, under the same flow conditions, small particles can more easily follow the streaming flows away from the wall and are re-entrained faster into the core flows when compared with larger particles. The gravitational sedimentation effect of large particles, however, reduces their rate of dispersion away from the wall.

Figure 13 also shows that the mean-σ for the 0.14 μm particles becomes smaller than the sample absolute minimum for $t^+ \geq 45$. This is because of dispersion of particles in the core region. Thus,

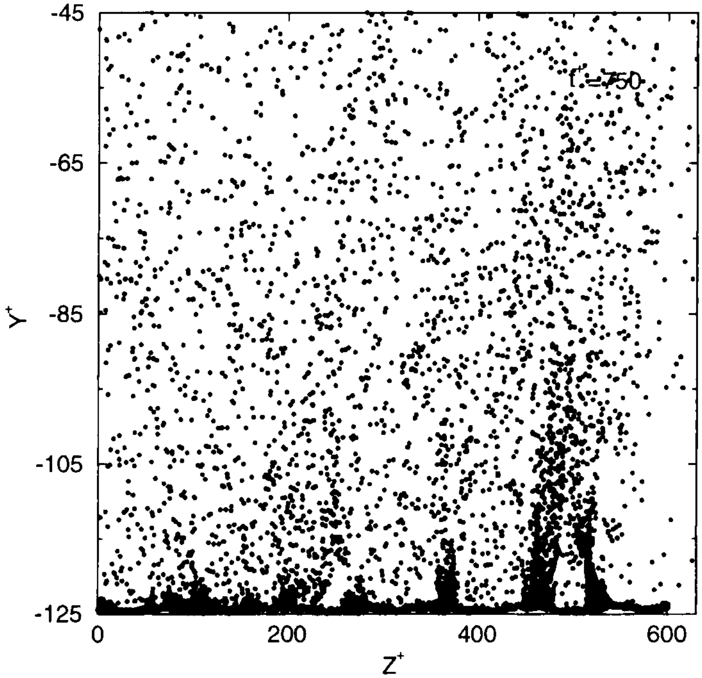

FIGURE 10c Distribution of 0.14 μm particles in the y–z plane at $t^+ = 750$.

σ becomes quite large and the mean-σ curve crosses the absolute minimum curve.

Velocity Statistics

In this section, simulation results for the mean and root-mean-square (RMS) velocities of 0.14 μm($\tau_p^+ = 0.023$), 3.21 μm($\tau_p^+ = 5$) and 40 μm($\tau_p^+ = 780$) particles during the re-entrainment process are reported. For each size, an ensemble of 8192 particles is initially uniformly distributed on a plane at a distance of 1.5 wall units from the lower wall. The particle mean and RMS velocities with the distance from the lower wall are obtained *via* averaging over a distance of 630 wall units in the streamwise direction for a time period of 0 to 100 wall units. Variations of the mean streamwise particle velocities with distance from the wall are shown in Figure 14a and are compared with the fluid velocity. It is observed that the mean streamwise particle

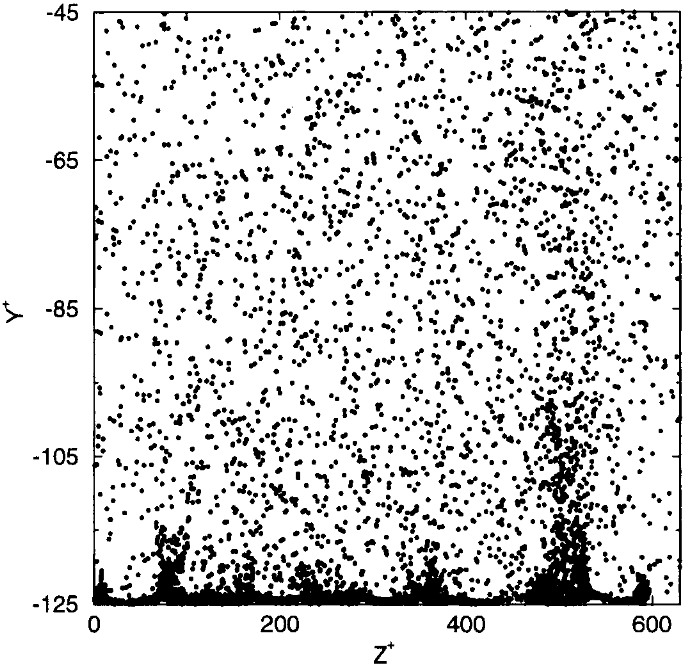

FIGURE 10d Distribution of 0.14 μm particles in the $y-z$ plane at $t^+ = 1000$.

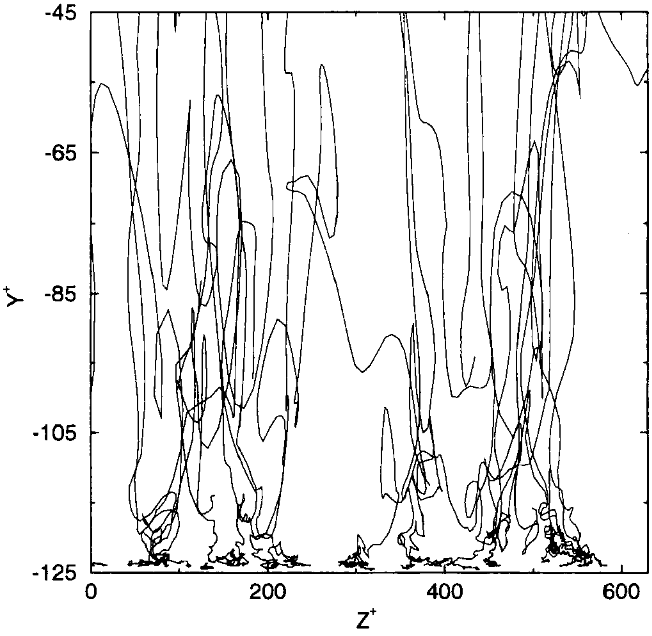

FIGURE 11a Sample 0.14 μm particle trajectories in the $y-z$ plane.

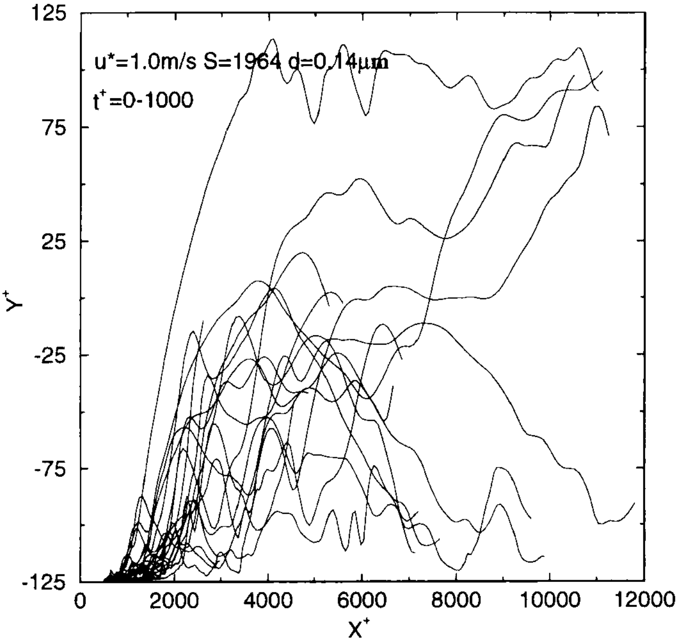

FIGURE 11b Sample 0.14 μm particle trajectories in the $x-y$ plane.

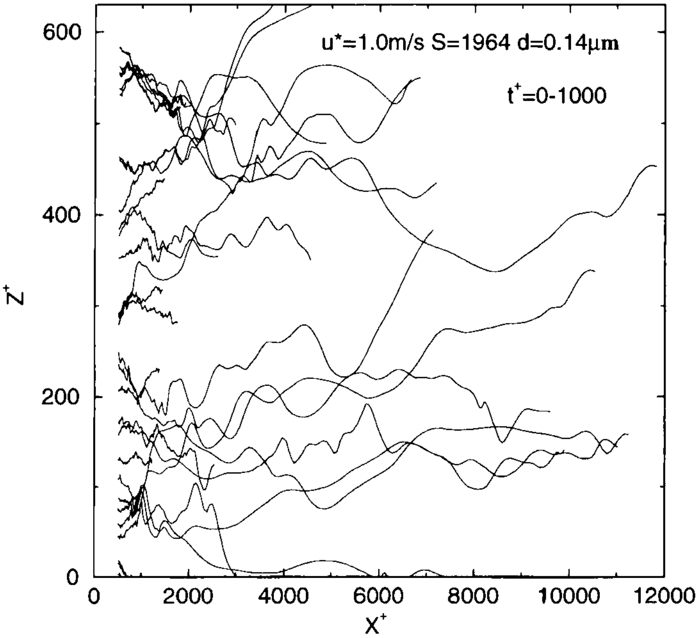

FIGURE 11c Sample 0.14 μm particle trajectories in the $x-z$ plane.

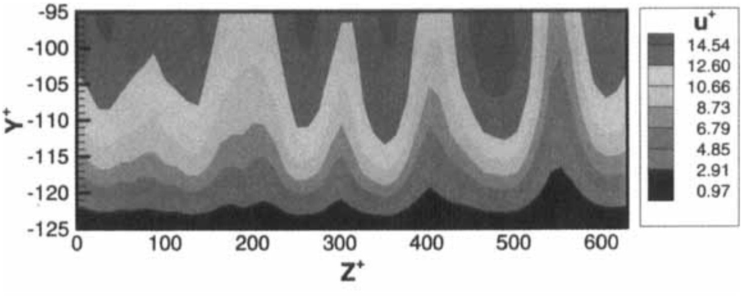

FIGURE 12a Contour plot of the mean *u*-velocity in the *y*–*z* plane. (See Color Plate VII).

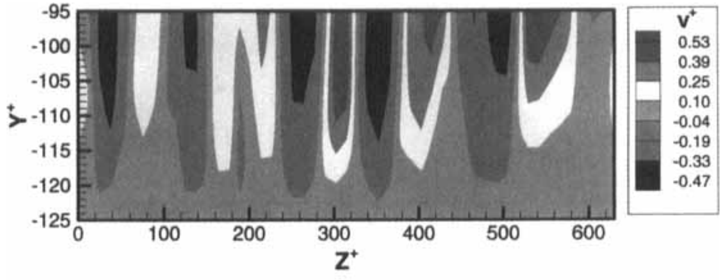

FIGURE 12b Contour plot of the mean *v*-velocity in the *y*–*z* plane. (See Color Plate VIII).

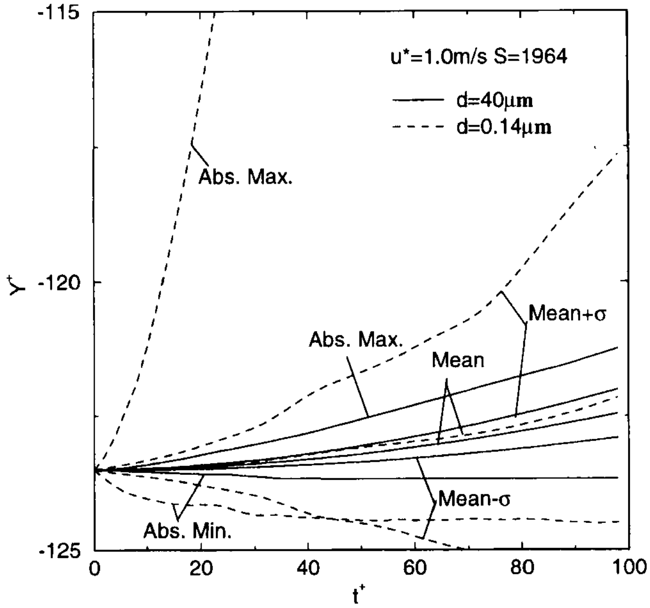

FIGURE 13 Trajectory statistics for 40 and 0.14 μm particles released from a plane source.

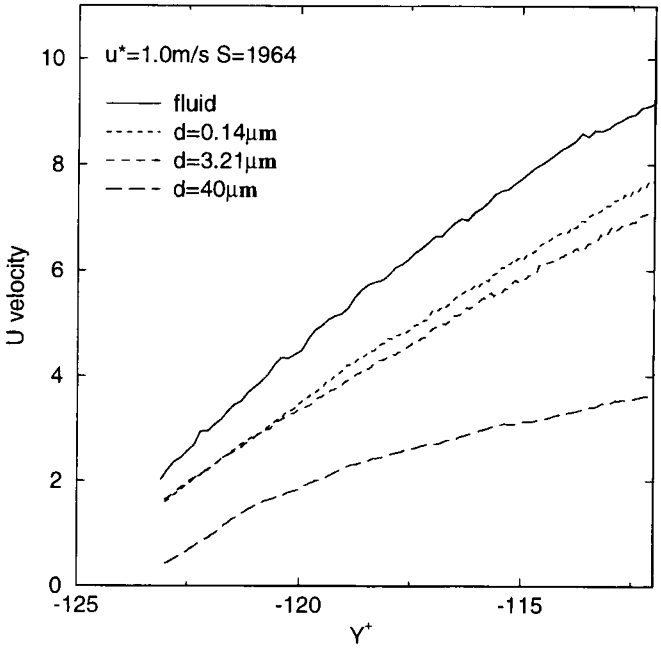

FIGURE 14a Variations of mean velocities of fluid and particles near the wall.

velocities are generally lower than that of the fluid, and smaller particles move faster than the larger ones in the streamwise direction. This is because particles are released very near the wall, and they move away from the wall by the upward motion of the near-wall eddies (for small particles) or by the lift force. (for large size particles). Thus, they carry lower streamwise velocities compared with that of the surrounding fluid.

RMS velocities for the fluid and different size particles are shown in Figure 14b. This figure shows that the RMS velocities of particles are lower than that of the fluid, and the smaller particles have larger RMS velocities compared with those of larger particles. The trend of variation of RMS particle velocities with distance from the wall is similar to that of the fluid. The exception is the streamwise RMS of 40 μm particles that increases up to about 3 wall units away from the wall and then decreases gradually. This may be due to the effect of the initial condition of these large particles with $\tau_p^+ = 780$ and the fact

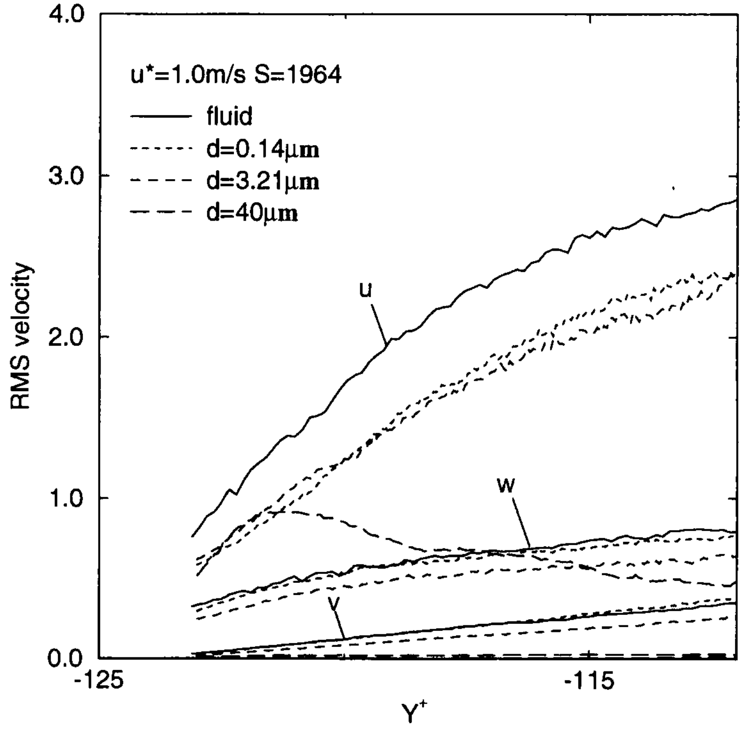

FIGURE 14b Variations of RMS velocities of fluid and particles near the wall.

that very few particles move away from the wall in the time duration of 100 wall units.

Mean Force

The statistics of various nondimensional forces acting on particles during the re-entrainment process are described in this section. Conditions of these numerical experiments are the same as those in the previous section. At every time step, ensemble averages of the y-component of drag, the lift forces, and the absolute value of Brownian and drag forces acting on particles that are moving in the region within 12 wall units from the lower wall are computed. (Positive sign denotes the direction is away from the lower wall.) The simulation results for the time duration of 50 to 100 wall units are shown in Figure 15.

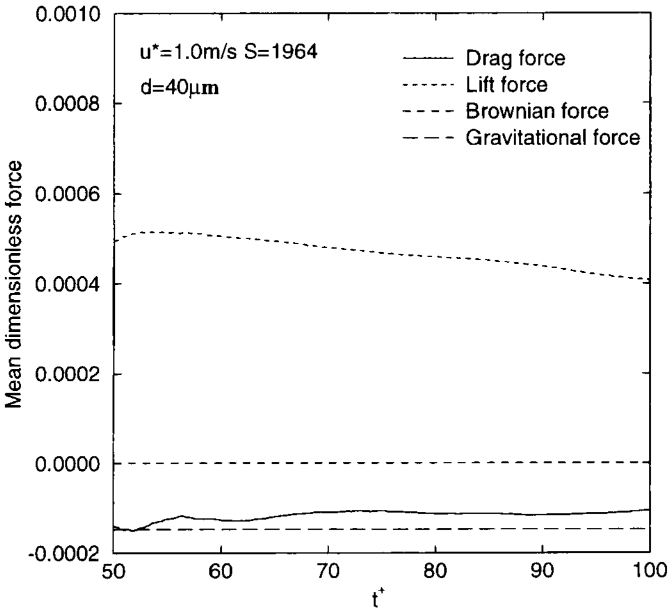

FIGURE 15a Time variations of averaged forces in the cross stream direction for 40 μm particles.

(The time after the startup to 50 wall units is omitted to eliminate the effect of initial conditions.)

Figure 15a shows the variation of various forces for 40 μm ($\tau_p^+ = 780$) in wall units. It is observed that the mean lift force is positive and relatively large indicating that the lift force makes particles move away from the wall. As noted before, this is the main mechanism for large size particle re-entrainment in turbulent flows. The mean drag force in the y-direction is negative, which also indicates that the particles are moving away from the wall. The magnitude of gravity is comparable with that of the mean drag force in this figure, and it also opposes the particle movement away from the wall. Figure 15a also shows that the Brownian force is negligible for 40 μm particles.

For 0.14 μm particles ($\tau_p^+ = 0.023$), Figure 15b shows the variation of averaged values of the Brownian, the drag, the lift and the gravitational forces. It is observed that the Brownian force plays an important role on the small-particle transport process. The lift force

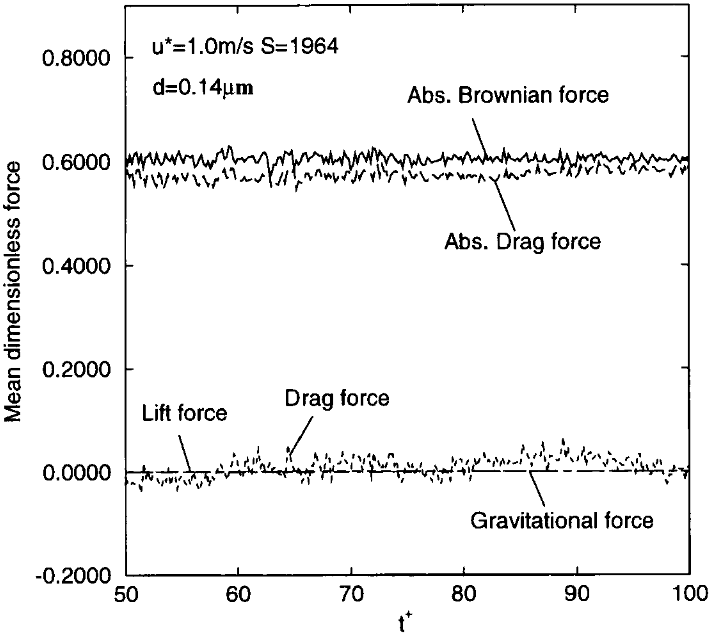

FIGURE 15b Time variations of averaged forces in the cross stream direction for 0.14 μm particles.

and the gravitational force for 0.14 μm particles are negligibly small. The mean absolute value of drag force is comparable with that of the Brownian force. The mean drag force, however, is oscillatory. These two figures also show that the magnitude of nondimensional drag force acting on 0.14 μm particles is about of an order of magnitude larger than that for 40 μm particles due to the significance of Brownian motion.

CONCLUSIONS

In this work, particle removal mechanisms from smooth surfaces in turbulent channel flows are studied. The theories of rolling and sliding detachments are used, and the particle removal process is studied. The effects of various forces, as well as near-wall turbulence flow structures are investigated. An ensemble of 8192 particles are used in these simulations for studying the re-entrainment process for each size and flow condition. Based on the present results, the following conclusions are drawn:

Removal and Adhesion

- The rolling detachment is the dominant mechanism for particle removal in turbulent flows.
- Drag and hydrodynamic torques are dominant, and the effect of lift and gravitational forces on particle detachment from the wall are negligible.
- The turbulence near-wall flow structure plays an important role in the particle detachment process.
- The simulated resuspension rates are in good agreement with the trend of model predictions of Reeks *et al.* [31]

Re-entrainment

- The instantaneous particle distribution in the $y-z$ plane during the re-entrainment process forms a periodic spanwise structure due to the turbulence near-wall coherent eddies.
- The present DNS of turbulent near-wall flows further shows that high-speed streamwise velocities correspond to those of downward flows (toward the wall), and the low-speed streamwise velocity regions correspond to upward flows (away from the wall).
- Turbulence near-wall flow structure plays an important role in both large and small particle re-entrainment processes but with different mechanisms.
- Large particles of the order of $d = 40\,\mu\text{m}$ ($\tau_p^+ = 780$) move roughly straight from the wall up to about 10 wall units due to the lift force, and then begin to disperse. These particles move away from the wall faster in the high-speed streamwise flow regions.
- Small particles follow the near-wall upward flows formed by the coherent near-wall vortices in the low-speed streamwise velocity regions during their re-entrainment process.
- Large particle dispersion perpendicular to the wall is slower than that for small particles due to the gravitational sedimentation effect and particle inertia.

- Particles move slower than the surrounding fluid in the streamwise direction and experience a lift force in the direction away from the wall.
- Small particles generally move faster than larger ones in the flow direction.
- For large particles, the Brownian force is negligible, and the Brownian motion is the dominating dispersion mechanism for small particles in the vicinity of the wall.

Acknowledgments

The authors would like to thank Professor John McLaughlin. This work was supported by the U.S. Department of Energy and New York State Science and Technology Foundation through the Center for Advanced Materials Processing (CAMP) of Clarkson University. The use of the NSF National Supercomputer Facility of the San Diego University is also gratefully acknowledged.

References

[1] Mittal, K. L., Ed., *Particles on Surfaces: Detection, Adhesion and Removal* **1–3**, (Plenum Press, New York, 1988, 1989, 1991).

[2] Corn, M., In: *Aerosol Sci.*, Davies, C. N. Ed. (Academic Press, New York, 1966), p. 359.

[3] Krupp, H., "Particle adhesion: Theory and Experiment", *Adv. Colloid Interface Sci.* **1**, 111–140 (1967).

[4] Visser, J.,"Adhesion of colloidal particles", In: *Surface and Colloid Sci.*, Matijevic, E. Ed., **8**, 3–84 (1976).

[5] Tabor, D., *Fluid Dynamics of Multiphase Systems* (Blaisdell Pub. Co., 1977).

[6] Bowling, R. A., "An analysis of particle adhesion on semiconductor surfaces", *J. Electrochem. Soc. Solid State Science Technol.* **132**, 2208–2219 (1985).

[7] Ranade, M. B., "Adhesion and removal of fine particles on surfaces", *J. Aerosol Sci. and Technol.* **7**, 161–176 (1987).

[8] Derjaguin, B. V., "*Untersuchungen ü ber die Reibung und adhäsion*", *IV*, *Koll. Z.* **69**, 155–164 (1934).

[9] Johnson, K. L., Kendall, K. and Roberts, A. D., "Surface energy and contact of elastic solids", *Proc. Royal. Soc. Lond.* **324**, 301–313 (1971).

[10] Derjaguin, B. V., Muller, V. M. and Toporov, Y. P. T., "Effect of contact deformation on the adhesion of particles", *J. Colloid Interface Sci.* **53**, 314–326 (1975).

[11] Muller, V. M., Yu, V. S. and Derjaguin, B. V., "On the influence of molecular forces on the deformation of an elastic sphere and its sticking to a rigid plane", *J. Colloid Interface Sci.* **77**, 91–101 (1980).

[12] Muller, V. M., Yu, V. S. and Derjaguin, B. V., "General theoretical consideration of the influence of structure forces on contact deformations and the reciprocal adhesion of elastic spherical particles", *J. Colloid Interface Sci.* **92**, 92–101 (1983).

[13] Maugis, D., "Adhesion of spheres: The JKR-DMT transition using a Dugale model", *J. Colloid Interface Sci.* **150**, 243–269 (1992).

[14] Maugis, D. and Pollock, H. M., *Acta Metall.* **32**, 1322 (1984).

[15] Tsai, C. J., Pui, D. Y. H., and Liu, B. Y. H., "Elastic flattening and particle adhesion", *J. Aerosol Sci. Technol.* **15**, 239–255 (1991).

[16] Rimai, D. S., DeMejo, L. P. and Verrland, W., "The effect of Young's modulus on the Surface–Force–Induced contact radius of spherical particles on polyurethane substrates", *J. Appl. Phys.* **71**, 2253–2258 (1992).

[17] Soltani, M. and Ahmadi, G., "Particle removal mechanism under base acceleration", *J. Adhesion* **44**, 161–175 (1994a).

[18] Soltani, M. and Ahmadi, G., "Particle detachment mechanisms from rough surfaces under substrate acceleration", *J. Adhesion Sci. Technol.* **9**(4), 453–373 (1995).

[19] Hinze, J. O., *Turbulence* (McGraw-Hill, New York, 1975).

[20] Ahmadi, G., "Overview of digital simulation procedures for aerosol transport in turbulent flows", In: *Particles in Gases and Liquids 3: Detection, Characterization, and Control*, Mittal, K. L. Ed. (Plenum, New York, 1993).

[21] Healy, J. W., "A review of resuspension models", In: *Transuranics in Natural Environments*, White, M. G. and Dunaway, P. B. Eds. (USERDA, Las Vegas, Nevada, 1977), pp. 211–222.

[22] Sehmel, G. A., "Particle resuspension: A review", *Environ. Int.* **4**, 107–127 (1980).

[23] Nicholson, K. W., "A review of particle resuspension", *Atmospheric Environment* **22**, 2639–2651 (1988).

[24] Smith, W. J., Whicher, F. W. and Meyer, H. R., "Review and Categorization of saltation, suspension and resuspension models", *Nuclear Safety* **23**, 685–699 (1982).

[25] Braaten, D. A., Paw, U. K. T. and Shaw, R. H., "Coherent turbulent structures and particle detachment in boundary layer flows", *J. Aerosol Sci.* **19**, 1183–1186 (1988).

[26] Yung, B. P. K., Merry, H. and Bott, T. R., "The role of turbulent bursts in particle re-entrainment in aqueous system", *Chem. Engng. Sci.* **44**, 873–882 (1989).

[27] Cleaver, J. W. and Yates, B., "Mechanism of detachment of colloid particles from a flat substrate in turbulent flow", *J. Colloid Interface Sci.* **44**, 464–474 (1973).

[28] Cleaver, J. W. and Yates, B., "A sublayer model for deposition of the particles from turbulent flow", *Chem. Eng. Sci.* **30**, 983–992 (1975).

[29] Cleaver, J. W. and Yates, B., "The effect of re-entrainment on particle deposition", *Chem. Eng. Sci.* **31**, 147–151 (1976).

[30] Reeks, M. W., Reed, J. and Hall, D., "On the resuspension of small particles by a turbulent flow", *J. Phys. D: Appl. Phys.* **21**, 574–589 (1988).

[31] Reeks, M. W. and Hall, D., "Deposition and resuspension of gas borne particles in recirculating turbulent flows", *J. Fluid Engng.* **110**, 165–171 (1988).

[32] Wen, H. Y. and Kasper, G., "On the kinetics of particle re-entrainment from surfaces", *J. Aerosol Sci.* **20**(4), 483–398 (1989).

[33] Wang, H. C., "Effect of inceptive motion on particle detachment from surfaces", *J. Aerosol Sci. Technol.* **13**, 386–396 (1990).

[34] Masironi, L. A. and Fish, B. R., "Direct observation of particle re-entrainment from surfaces", In: *Surface Contamination*, Fish, B. R. Ed., *Proc. of a Symp. at Gatlinburgh, Tennessee* (Pergamon Press, oxford, 1967), pp. 55–59.

[35] Soltani, M. and Ahmadi, G., "On particle adhesion and removal mechanisms turbulent flows", *J. Adhesion Sci. Tech.* **8**, 763–785 (1994).

[36] Soltani, M. and Ahmadi, G., "Particle detachment from rough surfaces in turbulent flows", *J. Adhesion* **51**, 105–123 (1995).

[37] McLaughlin, J. B., "Aerosol particle deposition in numerically simulated turbulent channel flow", *Phys. Fluids* **A1**, 1211–1224 (1989).

[38] Ounis, H., Ahmadi, G. and McLaughlin, J. B., "Dispersion and deposition of Brownian particles from point sources in a simulated turbulent channel flow", *J. Colloid Interface Sci.* **147**, 233-250 (1991).

[39] Ounis, H., Ahmadi, G. and McLaughlin, J. B., "Brownian particle deposition a directly simulated turbulent channel flow", *Phys. Fluids* **A5**, 1427-1432 (1993).

[40] Brooke, J. W., Kontomaris, K., Hanratty, T. J. and McLaughlin, J. B., "Turbulent deposition and trapping of aerosols at a wall", *Phys. Fluids* **A4**, 825-834 (1992).

[41] Pedinotti, S., Mariotti, G. and Banerjee, S., "Direct numerical simulation of particle behavior in the wall region of turbulent flows in horizontal channels", *Int. J. Multiphase Flow* **18**, 927-941 (1992).

[42] Soltani, M. and Ahmadi, G., "Direct numerical simulation of particle entrainment in turbulent channel flow", *Phys. Fluids* **7**, 647-657 (1995).

[43] Squires, K. D. and Eaton, J. K., "Measurements of particle dispersion obtained from direct numerical simulations of isotropic turbulence", *J. Fluid Mechanics* **226**, 1-35 (1991).

[44] Squires, K. D. and Eaton, J. K., "Preferential concentration of particles by turbulence", *Physics of Fluids* **A3**, 1169-1178 (1991b).

[45] Rashidi, M., Hetsroni, G. and Banerjee, S., "Particle-turbulent interaction in a boundary layer", *Int. J. Multiphase Flow* **16**(6), 935-949 (1990).

[46] Kim, J., Moin, P. and Moser, R., "Turbulent statistics in fully developed channel flow at low Reynolds number", *J. Fluid Mechanics* **177**, 133-166 (1987).

[47] Zhang, H. and Ahmadi, G., "Particle transport and deposition in vertical and horizontal turbulent duct flows", *J. Fluid Mechanics* **406**, 55-80 (2000).

[48] Goldman, A. J., Cox, R. G. and Brenner, H., "Slow viscous motion of a sphere parallel to a plane wall - II. Couette flow", *Chem. Engng. Sci.* **22**, 653-660 (1967b).

[49] Hinds, W. C., *Aerosol Technology, Properties, Behavior and Measurement of Airborne Particles* (John Wiley and Sons, New York, 1982).

[50] Clift, R., Grace, J. R. and Weber, M. E., *Drops and Particles* (Academic Press, New York, 1978).

[51] Goldman, A. J., Cox, R. G. and Brenner, H., "Slow viscous motion of a sphere parallel to a plane wall - I. Motion through a quiescent fluid", *Chem. Engng. Sci.* **22**, 637-651 (1967).

[52] Brenner, H., "The slow motion of a sphere through a viscous fluid towards a plane surface", *Chem. Eng. Sci.* **16**, 242-251 (1961).

[53] Li, Y., "Simulation of particle-laden channel flow with two-way coupling", *M. S. Dissertation*, Department of Chemical Engineering, Clarkson University (1998).

[54] Cox, R. G. and Brenner, H., "The slow motion of a sphere through a viscous fluid towards a plane surface - II. Small gap widths, including inertial effects", *Chem. Eng. Sci.* **22**, 1753-1777 (1967).

[55] O'Neill, M. E., "A sphere in contact with a plane wall in a slow linear shear flow", *Chem. Engng. Sci.* **23**, 1293-1298 (1968).

[56] Saffman, P. G., "The lift on a small sphere in a slow shear flow", *J. Fluid Mech.* **22**, 385-400 (1965).

[57] Saffman, P. G., Corrigendum to "The lift on a small sphere in a slow shear flow", *J. Fluid Mech.* **31**, 264 (1968).

[58] McLaughlin, J. B., "Inertial migration of a small sphere in linear shear flows", *J. Fluid Mech.* **224**, 261-274 (1991).

[59] Vasseur, P. and Cox, T. G., "The lateral migration of a spherical particle sedimenting in a stagnant bounded fluid", *J. Fluid Mech.* **80**, part 3, 561-591 (1977).

[60] Asmolov, E. S., "Transverse force acting on a spherical particle in a laminar boundary layer", *Izv. Akad. Nauk. SSSR Mekn. Zhidk. Gaza.* **5**, 66-71 (1989).

[61] McLaughlin, J. B., "The lift on a small sphere in wall-bounded linear shear flows", *J. Fluid Mech.* **246**, 249-265 (1993).

[62] Cox, R. G. and Hsu, S. K., "The lateral migration of solid particles in a laminar flow near a plane", *Int. J. Multiphase Flow* **3**, 201–222 (1977).

[63] Cherukat, P. and McLaughlin, J. B., "Wall induced lift on a sphere", *Int. J. Multiphase Flow* **16**, 899–907 (1994).

[64] Leighton, D. and Acrivos, A., "The lift on a small sphere touching a plane in the presence of a simple shear flow", *J. Applied Mathematics and Physics* (*ZAMP*), **36**, 174–178 (1985).

[65] Smith, C. R. and Schwartz, S. P., "Observation of streamwise rotation in the near-wall region of a turbulent boundary layer", *Phys. Fluid* **26**, 641–652 (1983).

[66] Acarlar, M. S. and Smith, C. R., "A study of hairpin vortices in a laminar boundary layer", Part II: Hairpin vortices generated by fluid injection, *J. Fluid. Mech.* **175**, 43–83 (1987).

[67] Robinson, S. K., "Kinematics of turbulent boundary layer structure", *Ph.D. Dissertation*, Stanford University (1990).